

General Disclaimer

One or more of the Following Statements may affect this Document

- This document has been reproduced from the best copy furnished by the organizational source. It is being released in the interest of making available as much information as possible.
- This document may contain data, which exceeds the sheet parameters. It was furnished in this condition by the organizational source and is the best copy available.
- This document may contain tone-on-tone or color graphs, charts and/or pictures, which have been reproduced in black and white.
- This document is paginated as submitted by the original source.
- Portions of this document are not fully legible due to the historical nature of some of the material. However, it is the best reproduction available from the original submission.

(NASA-TM-86162) INSTRUMENTAL BACKGROUND IN
BALLOON-BORNE GAMMA-RAY SPECTROMETERS AND
TECHNIQUES FOR ITS REDUCTION (NASA) 88 p
HC A05/MF A01 CSCL 03A

N85-18911

Uncias
G3/89 14157



Technical Memorandum 86162

INSTRUMENTAL BACKGROUND IN BALLOON-BORNE GAMMA-RAY SPECTROMETERS AND TECHNIQUES FOR ITS REDUCTION

N. Gehrels

January 1985

National Aeronautics and
Space Administration

Goddard Space Flight Center
Greenbelt, Maryland 20771



Instrumental Background in Balloon-Borne
Gamma-Ray Spectrometers and Techniques for Its Reduction

N. Gehrels

Laboratory for High Energy Astrophysics
NASA/Goddard Space Flight Center
Greenbelt, MD 20771

Accepted for publication in Nuclear Instruments and Methods
January 15, 1984

Abstract

A study of the instrumental background in balloon-borne gamma-ray spectrometers is presented. The calculations are based on newly available interaction cross sections and new analytic techniques, and are the most detailed and accurate published to date. Results compare well with measurements made in the 20 keV to 10 MeV energy range by the Goddard Low Energy Gamma-ray Spectrometer (LEGS). The principal components of the continuum background in spectrometers with Ge detectors and thick active shields are 1) elastic neutron scattering of atmospheric neutrons on the Ge nuclei, 2) aperture flux of atmospheric and cosmic gamma rays, 3) β^- decays of unstable nuclides produced by nuclear interactions of atmospheric protons and neutrons with Ge nuclei, and 4) shield leakage of atmospheric gamma rays. The improved understanding of these components leads to several recommended techniques for reducing the background. These include minimizing the passive material inside the shield and reducing the level of the shield threshold. A new type of coaxial n-type Ge detector with its outer contact segmented into horizontal rings can be used in various modes to reduce background in the 20 keV to 1 MeV energy range. The resulting improvement in instrument sensitivity to spectral lines is a factor of ~ 2 in this energy range.

CONTENTS

1. Introduction	3
2. Instrumentation and Observations	4
3. Background Components	6
3.1 Aperture Flux	7
3.2 Shield Leakage	9
3.3 Beta Decay	11
3.4 Elastic Neutron Scattering	16
3.5 Other Components	21
Continuum Due to Spectral Lines	
Electron Aperture Flux	
Proton Aperture Flux	
4. Background Reduction Techniques	24
4.1 Passive Material and Shield Threshold	24
4.2 Aperture Size	30
4.3 Detector Segmentation	32
5. Conclusions	40
Acknowledgements	43
Appendix	44
References	48
Tables	53
Figure Captions	63

1. Introduction

Due to the intense radiation environment at balloon and satellite altitudes and the weak source strengths of astronomical objects at gamma-ray energies, spectroscopic observations are necessarily background dominated in this energy range. Therefore, in addition to increasing detector volume, one can improve the sensitivity of gamma-ray spectrometers by decreasing the background level. One of the major challenges in designing new instruments is to find the optimum detector and shield configuration and to make the right materials choices to achieve a minimum background. To facilitate such design efforts, we have performed a study of the sources of background in balloon-borne Ge spectrometers operating in the 20 keV to 10 MeV energy range. The accuracy of this work was improved over previous studies by using several new measurements of atmospheric gamma-ray fluxes and nuclear interaction cross sections. The level of success of the calculations was determined by comparing to background measurements made during two balloon flights from Palestine, Texas in 1979 and 1980 by the Low Energy Gamma-ray Spectrometer (LEGS) [1], an instrument developed at NASA/GSFC in collaboration with groups at CENS and Rice University. In this paper we present the results of this study, and describe several ways in which instrumental background can be reduced in future instruments.

In general, the background in a balloon-borne gamma-ray spectrometer is made up of discrete background lines superimposed on a continuum. The origin of the lines is natural radioactivity of the materials in the instrument, activation of the instrument materials by atmospheric neutrons, and the annihilation of positrons produced in the instrument and the atmosphere by atmospheric radiations. The origin of the continuum is atmospheric and cosmic gamma rays that enter the instrument through its aperture or penetrate its

shield, and activation of the instrument materials by atmospheric neutrons and protons. Most of the lines in the background spectrum are intrinsically narrow, and therefore appear in the measured spectra with widths equal to the instrument resolution. This ranges from several keV FWHM for high-resolution Ge spectrometers such as LEGS to several tens of keV FWHM for instruments with scintillation-type detectors.

Many examples of observed high-resolution background spectra and line identifications can be found in the literature [1-7]. However, there are only a few published studies of the components that make up the background. For the continuum background there are three papers dealing with a phoswich scintillation detector [8-10] and one concerning a solid-state HgI_2 detector [11]. For the 511-keV background line there is one published study by Ling et al. [12] using data from a Ge detector. In this paper we present a detailed study of the continuum background in high-resolution Ge spectrometers and discuss techniques for its reduction. Preliminary results from this study have been given by Paciesas et al. [1] and Gehrels et al. [13].

2. Instrumentation and Observations

The LEGS instrument is described by Paciesas et al. [1]. In this section we will briefly review its general characteristics and give some details that are relevant for the background calculations. The instrument performs high-resolution spectroscopy between ~ 20 keV and 8 MeV using two interchangeable arrays of Ge detectors; the array chosen for a particular balloon flight depends on the observational goals. One array has three planar detectors of 1 cm thickness, 53 cm^2 total effective area below 100 keV (as viewed through the aperture collimator discussed below), and 57 cm^3 total active volume. Their efficiency is approximately unity between 20 and 100 keV, but drops steeply

above 100 keV. The other array has three coaxial detector of $\sim 230 \text{ cm}^3$ total active volume and 35.5 cm^2 peak effective area at 130 keV. The effective area decreases below 70 keV due to the top 1.4 mm Ge deadlayer typical of p-type coaxial detectors, and decreases above 200 keV due to the finite thickness of the detectors (4.6 cm). The decrease above 200 keV is less steep than that of the planar array, with the coaxial effective area at 1 MeV still 7.3 cm^2 .

For both arrays, the Ge detectors are cooled to liquid nitrogen temperatures. This is accomplished by enclosing them in an evacuated cryostat and thermally connecting them to a dewar of liquid nitrogen by a copper coldfinger. The detector and cryostat are situated inside an active NaI scintillator well to shield against cosmic rays and atmospheric radiations. The shield is $\sim 13 \text{ cm}$ thick, and collimates the field-of-view of the detectors to 16° FWHM. For the planar detectors, a passive Fe collimator is inserted inside the shield to additionally collimate the field-of-view to $5^\circ \times 10^\circ$ FWHM. The aperture solid angle per detector is given in Table 1 for the two LEGS flights for which background measurements are presented in this paper. Also listed in the table are the thresholds that were set on the shield pulse heights for the flights. Generally speaking, any photon or particle that deposits more energy than the threshold anywhere in the shield within $\sim 2 \mu\text{s}$ of a detector event vetoes that event. For the actual shield, nonuniformities in light collection from different regions of the NaI scintillator and suspected baseline shifts in the NaI photomultiplier tube amplifiers during the flight raised the effective thresholds in some regions by as much as a factor of ~ 2 .

Observations are performed by alternating every 20 minutes between pointing the detectors at a source and pointing at a region of sky without sources for background determination. The background measurements used for

comparison with calculations in this paper were obtained from background pointings in the time intervals listed in Table 1. The ranges of atmospheric depth and pointing angle for the instrument in these time intervals are also listed in the table.

As will be apparent in Section 3, an important contributor to the background in present instruments is the passive material inside the shield near the detectors. For LEGS, this includes the cryostat, the detector housings, inactive regions of Ge in the detectors, the section of coldfinger inside the shield, the inner walls of the shield housing, and the passive collimator for the planar detectors. Each material and its mass is listed in Table 2. Another quantity used in the calculations is the total instrument material in the field of view. For the coaxial array in flight III, this includes a 0.64 cm thick plastic scintillator at the top of the collimator and a 0.051 cm thick Al window on the pressure vessel. For the planar array in flight V, there was no scintillator, and the Al window on the pressure vessel was reduced to 0.038 cm. Both arrays also have material equivalent to 0.21 g cm^{-2} of air in their fields of view due to the air in the pressure vessel and the insulation around the pressure vessel. The cryostat window thickness is 0.17 cm Al for the coaxial array and $500 \text{ }\mu\text{m}$ Be for the planar array. The effective area plot in Paciasas et al. [1] includes the cryostat windows, but none of the other materials.

3. Background Components

In this section we discuss in detail the various components of the instrumental continuum background. The contribution of each component to the background of the LEGS instrument is calculated and compared to the measured background in flights III and V. Figures 1 and 2 show the measured background

spectra for the two flights, obtained with instrument parameters and time intervals listed in Table 1. The data include only those events for which there was no simultaneous shield veto, since events with vetoes are excluded from source observations and therefore do not contribute to the background for the source measurements. As discussed in Section 1, a large number of background lines can be seen in both spectra. The anticoincidence shield surrounding the detectors suppresses the escape peaks and Compton continuum from these lines, although there is a small contribution as discussed in Section 3.5. In this paper we are calculating the level of the continuum background in the spectra, which is approximately equal to the background in the intervals between the lines in the measured spectra. The solid, dashed, and dotted curves in Figures 1 and 2 show the results of the calculations described below.

3.1 Aperture Flux

At low energies ($\lesssim 150$ keV), a major source of background in both the coaxial and planar arrays is atmospheric and cosmic gamma rays that enter the instrument aperture and interact in one or more of the detectors. The photon need not deposit all of its energy in the detectors, but may also interact in passive material near the detectors, or even in the shield itself as long as the energy deposited does not exceed the shield threshold.

The contribution from gamma-ray aperture flux was calculated using a modified version of the UCSD Monte Carlo photon/electron transport code [9] to simulate the interaction of gamma rays with the LEGS instrument. The incident downward gamma-ray flux over Palestine, Texas at 5 g cm^{-2} for the coaxial data and 3.5 g cm^{-2} for the planar data was estimated from measurements that have been made at balloon altitudes over the last decade. The available data at 5

g cm⁻² is summarized in Figure 3. The spectrum used for the calculations is indicated by the solid line, and represents power-law fits to the combined data of Kinzer [14], Kinzer et al., [15], and Schönfelder et al. [16]. A similar analysis at 3.5 g cm⁻² gives power law fits (ph cm⁻² sr⁻¹ s⁻¹ MeV⁻¹) of $2.19 \times 10^2 E^{0.70}$ between 0.024 and 0.035 MeV and $5.16 \times 10^{-2} E^{-1.81}$ between 0.035 and 10 MeV. The downward gamma-ray flux was used in this analysis, even though the pointing angle of the telescope during the background measurements reached values as large as 54° from zenith (see Table 1). However, this should result in only a small error since the total gamma-ray flux is approximately independent of angle between 0° and 70° [18, 21].

The calculated contributions of the aperture flux to the continuum backgrounds for the coaxial and planar detectors are shown by the long-dashed curves in Figures 1 and 2 respectively. For the coaxial detectors there is an uncertainty of $\pm 15\%$ in this component due to uncertainties in our knowledge of the thickness of the inner Al wall of the shield housing (see Table 2) and of the actual shield threshold during the flight (100-200 keV). For the planar detectors, the same uncertainties in the shield housing and threshold exist, but the resulting uncertainty in the aperture flux curve from this source is only approximately $\pm 5\%$. This is because the Fe collimator tubes used in the planar configuration are the dominant passive material inside the shield and because the tubes tend to block low-energy secondary photons from interacting in the shield.

The aperture flux curves in Figures 1 and 2 are broader and higher than one would calculate assuming a 0 keV shield threshold and no passive material inside the shield. This effect will be discussed in detail in Section 4.1. For the coaxial detectors the aperture flux is the largest component between 70 and 150 keV, and for the planar detector it is the largest component between 30 and 100 keV.

3.2 Shield Leakage

The other background component due to gamma rays is the shield leakage. In this case, the background is caused by the small fraction of atmospheric gamma rays that manage to leak through the shield without depositing more energy in it than the shield threshold, and then interact in the detectors. The shield leakage contribution to the coaxial and planar detector background was calculated using the photon/electron transport code to simulate the interactions of the incident gamma rays with the instrument.

The zenith angle distribution of the total gamma-ray flux at MeV energies in the atmosphere has been shown by Schönfelder et al. [21] and others to be essentially flat between 0° and 70° (0° = downward moving photons), rising by a factor of ~ 4 to a peak at 110° , and then falling by a factor of ~ 2 to a plateau between 130° and 180° . The actual spectra used as input for our calculations were based on the measured downward fluxes described in Section 3.1 and on measurements at 112° and 164° obtained at 2.5 g cm^{-2} atmospheric depth by the Max Planck gamma-ray telescope [21]. The measurements at 2.5 g cm^{-2} were corrected to 5 g cm^{-2} (coaxial detectors) and 3.5 g cm^{-2} (planar detectors) with the calculated depth dependences of Ling [18]. Specifically, the forms for the differential spectrum ($\text{ph cm}^{-2} \text{ sr}^{-1} \text{ s}^{-1} \text{ MeV}^{-1}$) used in various angular regions at 5 g cm^{-2} were $0.059 E^{-1.75}$ for 0° to 65° (Figure 3), $0.094 E^{-1.61}$ for 65° to 95° , $0.15 E^{-1.47}$ for 95° to 130° , and $0.047 E^{-1.45}$ for 130° to 180° . At 3.5 g cm^{-2} they were $0.052 E^{-1.81}$ for 0° to 65° , $0.085 E^{-1.66}$ for 65° to 95° , $0.14 E^{-1.50}$ for 95° to 130° , and $0.047 E^{-1.45}$ for 130° to 180° .

There are several uncertainties in these spectra. The power-law forms were assumed in our analysis to apply over the energy range 0.1 to 10 MeV, while they were measured only in the 1.5 to 10 MeV range [21]. We feel this

is not a major problem because, in the energy range of most uncertainty (below ~ 0.5 MeV), the dominant shield leakage background is due to higher-energy photons that are scattered in passive materials near the detectors; the direct leakage of atmospheric photons is cut off below 0.5 MeV by the increasing absorption cross section of the shield. Another problem is that a more recent flight of the Max Planck gamma-ray telescope [16] indicated that the spectra presented in their 1977 paper (ref. 21; i.e., those used in our analysis) were low by a factor of 1.5 to 2 above ~ 5 MeV due to an overestimate of the background in that energy range. Unfortunately, angular distributions are not given for the later flight. It is therefore possible that the shield leakage background component in the present calculations is low above ~ 5 MeV.

In the calculations, the simplifying assumption was made that the instrument pointed straight upward throughout the background measurements, although it was actually pointed more typically 20° to 40° from zenith. We expect the inaccuracy in the results due to the pointing to be small ($\ll 30\%$), because there is a cancellation of effects. As the instrument tilts, the detectors see an increase in shield leakage through one side of the shield as the thin upper section moves between them and the large flux at 90 - 110° , but at the same time they see a decrease through the opposite side of the shield as the thick lower section moves to 90° .

The shield leakage component is shown by the short-dashed curves in Figures 1 and 2. The uncertainty in the plotted curves is estimated to be $\pm 50\%$ at 40 keV and $\pm 20\%$ at 1 MeV for the coaxial detectors (Figure 1), and \pm factor 2 at 40 keV and $\pm 40\%$ at 1 MeV for the planar detectors (Figure 2). The shield leakage is seen to be a major component over most of the energy range of both detector arrays. For the coaxial array, the shield leakage is virtually the only component above 2 MeV. The fit to the observed background

spectrum in this energy range is seen in Figure 1 to be very good, indicating that the shield leakage component is well determined by the above calculation technique. The agreement with the data is in fact fortuitously good given the input spectrum uncertainties and uncertainties in the shield threshold and wall thickness. As in the case of the aperture flux, the nonzero shield threshold and the passive material inside the shield cause an increase in the background, as will be discussed in Section 4.1.

3.3 Beta Decay

The β -decay background is due to the decay of β^- -unstable nuclides produced by nuclear interactions of atmospheric protons and neutrons with Ge atoms in the detectors. The signal in this case is produced by the ionization energy loss of the decay electron as it stops in the detector. Since the typical β^- -decay lifetimes are much longer than the microsecond coincidence times of the instrument, any interactions of the primary proton or neutron in the shield do not veto the event, and any energy deposition in the detector from the primary particle or the recoil of the Ge atoms is not included in the signal.

In many cases, the daughter nuclide of the β decay is produced in an excited state that decays in a time short compared with the coincidence time. Therefore, in addition to an electron and neutrino, these decays also have one or more prompt gamma rays and occasionally (internal conversion) another electron. For the case where no gamma rays are emitted (i.e., decays to the ground state or a metastable state of the daughter), the energy is deposited in a small localized region of the detector due to the small range of the decay electrons; for example, the range of a 1 MeV electron in Ge is

≤ 1 mm*. For the case where one or more prompt gamma rays are emitted, the event will fall in one of the following categories: 1) The gamma ray does not interact in the detector and does not deposit enough energy in the shield to exceed the threshold. The event is therefore accepted, and appears as a localized event. 2) The gamma ray deposits enough energy in the shield to exceed the threshold, causing the event to be vetoed. 3) The gamma ray interacts in the detector, but does not deposit enough energy in the shield to exceed the threshold. The event is accepted and the signal in the detector is the sum of the gamma-ray deposition and the β^- energy loss. Since the gamma-ray interaction is, in general, in a different region of the detector than the β^- decay, these events are called nonlocalized events.

Only β^- decays are discussed in this section, although β^+ decays can also produce background events. The continuum background contribution from β^+ decays in the detector was calculated and found to be extremely small, primarily because the events are suppressed by the photons produced when the positron annihilates. The annihilation produces two oppositely-directed 511-keV photons, at least one of which escapes the detector in almost all cases and interacts in the shield vetoing the event. The decays that proceed via electron capture do not produce positrons, and are therefore not vetoed by the annihilation radiation. However, these decays generally do not contribute to the continuum background since any prompt gamma rays absorbed in the detector will be in narrow background lines.

Since the β^- -decay lifetimes are much longer than the instrument coincidence times, the relevant particle spectra at the detectors should include all contributions from secondaries produced in the shield. In order to obtain these spectra, we followed the suggestion of Mahoney et al. [6] of

*The electron ranges used in this paper were calculated with formulas in Evans [22] for extrapolated ranges in Al, scaled to other materials using the relation $R(A,Z) = A/Z \cdot 13/27 \cdot R_{Al}$ given by Koral and Cohen [23].

using spectra measured in the atmosphere at a depth equal to that of the actual atmosphere above the instrument plus the equivalent depth of the shield. The LEGS shield is approximately 48 g cm^{-2} thick, which corresponds to 31 g cm^{-2} of air due to the difference in nuclear collision lengths (60.2 g cm^{-2} for air vs 91.1 g cm^{-2} for NaI [24]). Thus, with actual instrument atmospheric depths for the LEGS flights in the range 3 to 5 g cm^{-2} , the total effective atmospheric depth inside the shield is $\sim 35 \text{ g cm}^{-2}$.

The input neutron spectrum for this calculation was derived from those calculated by Armstrong et al. [25], which are consistent with observations and are presented in a convenient format. The specific spectrum we used is shown in Figure 4, and is a logarithmic interpolation to 35 g cm^{-2} between power-law representations of their spectra at 10 and 50 g cm^{-2} . The proton spectrum below 3.6 GeV (geomagnetic cutoff at Palestine) was more difficult to obtain because there are no recent calculations or published measurements. The approach taken was to use the equations of Rossi [26] for the atmospheric proton and neutron spectra, and determine the intensity constant in the equations by fitting the neutron spectrum to the one shown in Figure 4. The resulting proton and neutron curves are shown by dashed lines in the figure. The shape of the Rossi neutron spectrum is seen to be in reasonable agreement with that of the Armstrong et al. spectrum. The proton spectrum used in the β^- calculation is shown by the solid-line power-law curves, and was derived by matching the Armstrong et al. neutron spectrum above 300 MeV and following the shape of the Rossi proton spectrum at lower energies. There is one set of measurements by McDonald and Webber [27] of the integral proton flux between 100 and 750 MeV at a similar magnetic latitude as that of Palestine. The flux at 35 g cm^{-2} implied by their observations is $0.23 \text{ protons cm}^{-2} \text{ s}^{-1}$ assuming an isotropic flux distribution, which is in excellent agreement with the value

calculated from the power-law curves in Figure 4 of $0.25 \text{ protons cm}^{-2} \text{ s}^{-1}$. Above the geomagnetic cutoff at 3.6 GeV, the proton spectrum was taken to be the primary cosmic-ray spectrum measured by Webber and Lezniak [28] multiplied by a factor of 0.56 to account for protons lost to nuclear collisions in the atmosphere and in the shield.

An extensive literature search was performed to find the required interaction cross sections for protons and neutrons incident on the five naturally occurring Ge isotopes to produce β^- -unstable nuclides. For neutrons, several compilations of cross section data are available [29-32]. By far the most useful of these for our application was the compilation of Howerton, Dye, and Perkins [32] which has recently been revised to include data on Ge. For protons, the semiempirical cross sections of Silberberg and Tsao [33,34] were used. The calculations were greatly facilitated by a computer code provided to us by the authors giving their most recent cross sections. The accuracy of the present study would have been significantly poorer without the new neutron cross sections for Ge of Howerton, Dye, and Perkins, and without convenient access to the proton cross sections of Silberberg and Tsao.

The actual calculations are described in detail in the Appendix, and will only be summarized here. The β^- -activation rates were determined by integrating the neutron and proton spectra at the detectors with the interaction cross sections of each Ge isotope. All final states listed as β^- emitters in the Table of Isotopes [35] were considered, amounting to more than a hundred for each Ge isotope. Each activation rate was then multiplied by the β^- branching fraction and the decay mode fraction for each possible final state, to give the rates for the different decay modes of each nuclide produced. Decays accompanied by a prompt gamma ray were also multiplied by

another factor to eliminate events with interactions in the shield. It was assumed that any gamma ray not fully absorbed in the detector is vetoed by the shield. The efficiencies for internally-produced photons to be fully absorbed in the detectors were calculated using the Monte Carlo code. For LEGS this assumption gives an underestimate of the background produced by β^- decays accompanied by prompt gamma rays, since some of the photons escaping the detectors are absorbed in the passive materials near the detectors or interact in the shield without exceeding the high (~ 100 keV) threshold. However, the effect on the total background is negligible, because, as will be shown, the prompt gamma-ray decays are only a small fraction of the background. In later sections of the paper, these calculations will be repeated for future instrument configurations that have very little passive material near the detectors and low thresholds for the shield. In these cases the use of the total-absorption efficiency for the nonvetoed fraction is nearly correct, and the calculated rates for the β^- decays accompanied by prompt gamma rays should be accurate.

For each decay mode for each β^- -unstable nuclide produced, the β^- energy spectrum was determined using the rates calculated as described above and the β^- spectral shapes of Behrens and Szybisz [36]. The spectra were then summed to produce the total β^- -decay background spectrum in the detectors. More than 1000 production rates were calculated and 60 spectra summed to determine the final background spectrum. The results for the LEGS coaxial and planar detector arrays are shown by the dotted curves in Figures 1 and 2 respectively. For the coaxial array the background produced by the nonlocalized prompt gamma-ray decays is shown separately from the localized ground-state decays. For the planar array only the localized decays are included, because the prompt gamma rays from the nonlocalized decays typically

escape the thin detectors and interact in the shield, vetoing the event.

One of the new results obtained from this calculation is that the background from nonlocalized decays is extremely small - more than an order of magnitude less than the background from the localized decays. This is a somewhat surprising result given that $\sim 2/3$ of all β^- -decay nuclides that can be produced by neutron and proton interactions with Ge have a greater than 50% probability of emitting prompt gamma rays during the decay. The reason for this is twofold: first, by chance, the three most abundantly produced nuclides, namely ^{75}Ge , ^{70}Ga , and ^{69}Zn (see Table 4 and Figure 18), decay predominantly to the ground states of the daughter nuclides; second, the decays with prompt gamma rays are suppressed because many of the photons interact in the shield or produce secondaries that interact in the shield and veto the event.

The β^- -decay component is an important part of the total background between ~ 150 keV and ~ 1.5 MeV for the LEGS coaxial detectors, and above ~ 300 keV for the planar detectors. For future instruments with thicker shields and smaller apertures than LEGS, the β^- -decay component will dominate the background at intermediate energies, as will be shown in Section 4.3.

3.4 Elastic Neutron Scattering

The elastic neutron scattering background is due to the recoil of Ge atoms in the detectors following elastic scatterings with incident atmospheric neutrons. The signal from this interaction is prompt, so that only those neutrons that do not interact in the shield while entering or leaving the instrument contribute to the background. The calculation of this component was done by determining the spectrum at the detectors of neutrons that do not interact in the shield, and integrating the spectrum times the Ge elastic

scattering cross sections. The energy deposited in the detector was found by multiplying the recoil energy by the fraction of energy lost via signal-producing ionizing collisions in the detector.

For the incident neutron spectrum, we used power-law approximations of the calculated spectrum of Armstrong et al. [25] at 5 g cm^{-2} atmospheric depth. This spectrum was multiplied by a correction factor to eliminate neutrons that veto the background event upon entering or leaving the instrument by interacting in the NaI shield and depositing more energy than the shield threshold. To obtain this factor it was necessary to determine what kinds of interactions in the shield are capable of depositing more energy than the threshold. In particular, for elastic scattering, the recoil energy of the nucleus, E_R , is given by

$$E_R = \frac{2A}{(1+A)^2} (1 - \cos\theta) E_n \quad (1)$$

(see, e.g., ref. 37) where A is the mass of the target nucleus divided by the neutron mass, E_n is the incoming neutron kinetic energy in the lab frame, and θ is the scattering angle of the neutron in the center-of-mass frame. For Na, the maximum possible recoil energy is only 16% of the incident neutron energy, and, for I, only 3%. Thus, based on equation (1) alone, it can be seen that neutrons with energies less than 0.6 MeV can not exceed the $\sim 100 \text{ keV}$ shield threshold via elastic scatterings.

It can be shown, in fact, that even neutrons with energies in the 1-100 MeV range generally will not trigger the shield via elastic scatterings. This is because the elastic scattering cross sections at high energies are peaked near $\cos \theta = 1$ [38] and because, as will be discussed below, in this energy range more than half of the recoil energy is lost to interactions in the NaI

that do not produce detectable signals. Inelastic collisions, on the other hand, generally disrupt the target nuclei producing photons and/or particles with typical energies in the MeV range, and therefore almost always produce shield vetoes. Hence, we make the assumption that no elastic scatterings exceed the shield threshold but that all inelastic scatterings do. The interaction length due to inelastic scatterings (also known as the absorption length) in NaI is 41.3 cm [24], so that the fraction of incident neutrons that penetrate the ~ 13 cm thick LEGS shield twice (entering and leaving) without producing a veto is ~ 0.53 . In later sections of this paper, a new instrument will be considered with a 15.2 cm (6") thick NaI shield. For this case, the noninteracting fraction is 0.48. The actual neutron spectrum (neutrons $\text{cm}^{-2} \text{s}^{-1} \text{MeV}^{-1}$) at the detectors used in the LEGS calculations, including the 0.53 factor, is $0.053 E_n^{-0.93}$ between 0.1 and 100 MeV and $0.85 E_n^{-1.6}$ between 100 and 10^4 MeV.

The equation for calculating the counting rate per unit volume of Ge, per unit energy detected signal in the detector, $\frac{dR}{dE}$, for the elastic neutron scattering background is

$$\begin{aligned} \frac{dR}{dE} &= \frac{dE_R}{dE} \frac{dR}{dE_R} (E_R = E/f) \\ &= \frac{1}{f + df/dE_R \cdot E_R} \frac{10^{-27} \rho N_A}{w} \int_0^\infty \frac{d\sigma}{dE_R} j_n dE_n \quad \text{cnts s}^{-1} \text{MeV}^{-1} \text{cm}^{-3} \quad (2) \end{aligned}$$

where E is the energy collected as signal in the detector, E_R is the Ge atom recoil energy, f is the fraction of the recoil energy collected as signal ($= E/E_R$), ρ is the density of the target element (5.36 g cm^{-3} for Ge), N_A is $6.02 \times 10^{23} \text{ atoms mole}^{-1}$, w is the atomic weight of the target element (72.6 g mole^{-1} for Ge), $\frac{d\sigma}{dE_R}$ is the elastic scattering cross section per unit recoil

energy for incident neutrons of energy E_n in units of millibarns MeV^{-1} , 10^{-27} is the number of cm^2 per millibarn, and j_n is the neutron flux at the detector at energy E_n in units of $\text{cm}^{-2} \text{s}^{-1} \text{MeV}^{-1}$ (see above discussion). The cross-section data used in this analysis are given in terms of $\frac{d\sigma}{d\Omega}$ as a function of θ , so we take one more step, using equation (1) to convert from $\frac{d\sigma}{dE_R}$ to $\frac{d\sigma}{d\Omega}$, with the result for Ge

$$\frac{dR}{dE} = \frac{1.03 \times 10^{-2}}{f + df/dE_R \cdot E_R} \int_{18.5 E_R}^{\infty} \frac{d\sigma}{d\Omega} \frac{j_n}{E_n} dE_n \quad (3)$$

where the lower limit on the integral is the minimum energy neutron that can produce a Ge recoil of energy E_R , determined from equation (1).

The cross sections for elastic neutron scattering on Ge were obtained from the plots of Garber et al. [38]. The data are given in that compilation as plots of $\frac{d\sigma}{d\Omega}$ vs θ for various E_n . In order to convert to $\frac{d\sigma}{d\Omega}$ vs E_n for constant E_R (or E), one point was taken from each E_n plot at a value of θ determined using equation (1). The results for two example energies, $E_R = .04$ and $.17$ MeV, are shown by the filled circles in Figure 5. In both cases, there is not enough data on Ge to adequately define the shapes of the curves at energies greater than ~ 10 MeV. For this reason, we have used the more extensive data on Cu to indicate the shapes at higher energies. For each plot, the values of E_R for Cu were chosen such as to have the same $E_n \text{ min}$ as Ge. Specifically, we chose $E_R(\text{Cu}) = 1.138 E_R(\text{Ge})$ (equation (1) with $A(\text{Ge}) = 71.97$ and $A(\text{Cu}) = 63.00$). The cross sections for the Cu are shown as x's in Figure 5. For small values of $E_R(\text{Ge})$ near $.04$ MeV, the agreement between the Ge and Cu points is quite good in the energy range where both are measured, whereas for the larger values of $E_R(\text{Ge})$ near $.17$ MeV, there are some systematic disagreements in the trend of the points for the two elements of

typical magnitude 50%. The lines in Figure 5 are the power-law approximations to the cross-section curves that were used in the integral in equation (3). Approximately half of the contribution to the integral is from $E_n > 10$ MeV.

The final consideration in the elastic neutron scattering calculation is the fraction of the recoil energy that produces signal in the detector. Qualitatively, an elastic scattering interaction in a Ge crystal can be viewed as follows: The neutron enters the detector and scatters elastically off the nucleus of a Ge atom imparting a recoil kinetic energy to the atom nearly equal to the energy lost by the neutron (the displacement energy of a Ge atom from the lattice is only ~ 18 eV [39]). The Ge atom then loses its energy both via electronic collisions that produce ionization in the detector (collected as signal), and via atomic collisions that displace other atoms from the lattice. The atomic collisions do not produce ionization in the detector, although the displaced atoms can, in turn, lose part of their energy to electronic collisions. The total fraction of the recoil energy that is lost to signal-producing electronic collisions is denoted by f in equations (2) and (3).

The fraction f has been determined theoretically by Lindhard et al. [40], with the relevant equations given in a convenient format by Robinson [41]. The equation used for the present analysis is

$$f = \frac{k_L g(E_R/E_L)}{1 + k_L g(E_R/E_L)} \quad (4)$$

where $k_L = 0.134 Z^{2/3} A^{-1/2}$, $E_L = 86.93 Z^{7/3}$ eV, $g(\epsilon) = 3.401\epsilon^{1/6} + 0.402\epsilon^{3/4} + \epsilon$, Z is the atomic number, and A is the atomic mass. Figure 6 shows f as a function of recoil energy, E_R , for Ge. As an example using these data, we see that for the recoil energies of .04 and .17 MeV discussed in regard to

Figure 5, the measured energy in the detector is .012 and .066 MeV respectively.

Combining the neutron spectra, the elastic scattering cross sections, and the data in Figure 6 with equation (3), gives the elastic neutron scattering background components in Figures 1 and 2 for the LEGS coaxial and planar detector arrays. The main uncertainties in these curves comes from uncertainties in the cross-section data such as those shown in Figure 5. We estimate this uncertainty to be 20% at low energies ($E_R = .04$ MeV, $E = .012$ MeV) and 70% at higher energies ($E_R > .17$ MeV, $E > .066$ MeV). The elastic scattering component is seen to be important at low energies, exceeding even the aperture flux below 50 keV for the coaxial detectors and below 25 keV for the planar detectors.

3.5 Other Components

We now estimate the magnitude of several other components and show that their contributions to the background are small.

1. Continuum Due to Spectral Lines - The thick anticoincidence shield that is used to keep out atmospheric radiations in gamma-ray spectrometers also serves as an excellent veto for events with Compton-escape photons. However, the nonzero shield threshold and the passive material between the detectors and the shield, allow some such events to be included in the background. For the background components discussed so far, this effect has been included in the calculation, but there is an additional component due to the Compton continuum of the lines in the spectrum. We consider for example the line at 198 keV, which is the strongest line in the coaxial spectrum.

The interaction producing the 198 keV line is $^{70}\text{Ge}(n,\gamma)^{71m}\text{Ge}$. The

metastable state decays with a half-life of 22 ms yielding a 23 keV internal conversion electron and a 175 keV photon. Using laboratory data and Monte Carlo simulations we estimate (to within a factor of 2) that the continuum background below a line of this energy is ~ 4 cnts MeV⁻¹ per count in the line. There is some structure in this continuum such as a Compton edge and a broad backscatter peak, which we ignore for the purpose of this approximate calculation. For the coaxial detectors in flight III, the intensity in the 198 keV line was 0.65 cnts s⁻¹, giving a continuum background at energies less than 198 keV of $\sim 1.1 \times 10^{-2}$ cnts s⁻¹ MeV⁻¹ cm⁻³. Comparing with Figure 1, it is seen that the contribution is 10-20% of the observed background in this energy range. This component is not included in Figure 1 because the data were not available to perform an accurate calculation. In future instruments with thicker shields, less passive material near the detectors, and lower shield thresholds, this component should be negligible.

2. Electron Aperture Flux - The electron aperture flux background is due to primary and atmospheric-secondary electrons that enter the aperture of the instrument and stop in a detector. We obtain the incident flux in the upper atmosphere from the calculations of Daniel and Stephens [42], who treat both electrons and gamma rays with energies between 1 MeV and 10 GeV at all atmospheric depths. There is some disagreement between their gamma-ray spectra and observations below 1 GeV [43], but their electron spectra agree well with observations [44]. At 5 g cm⁻² atmospheric depth, the calculated electron intensity can be represented by $1.4 \times 10^{-2} E^{-1.8}$ electrons cm⁻² sr⁻¹ s⁻¹ MeV⁻¹ between 1 and 10 MeV, and is approximately isotropic below 5 MeV [42].

To set an extreme upper limit on the electron contribution to the

background, we assume that the spectrum between 1 and 10 MeV can be extrapolated as a power law to lower energies, and that there is no absorbing instrument material in the aperture. If these assumptions were valid, the electron background would be significant at low energies; for example, with an aperture solid angle of .08 sr and a detector area of $\sim 50 \text{ cm}^2$ the background for the coaxial detectors would be $.04 \text{ cnts s}^{-1} \text{ MeV}^{-1} \text{ cm}^{-3}$ at 60 keV, which is comparable to the aperture flux, although it would be only $2 \times 10^{-4} \text{ cnts s}^{-1} \text{ MeV}^{-1} \text{ cm}^{-3}$ at 1 MeV, which is small. The above assumptions, however, are not valid. The spectrum almost certainly falls below the power-law extrapolation at energies less than 1 MeV, because the electron range in the atmosphere becomes small at these energies. Also, the material in the path of the incoming electrons is thick to low energy electrons. The .17 cm thick Al window on the cryostat, by itself, stops electrons with energies less than $\sim 1 \text{ MeV}$. Including the Al pressure-vessel window, the plastic scintillator in the aperture, and the inactive layer of Ge on the detectors, the threshold energy for electrons to reach the active Ge for the coaxial detectors is over 3 MeV. Hence, the electron aperture flux is a negligible background component.

3. Proton Aperture Flux - The proton aperture flux background, due to atmospheric protons that enter through the instrument aperture and stop in the detectors, can be seen immediately to be a negligible component. First, the flux of protons is extremely small; even at 35 g cm^{-2} atmospheric depth, the intensity at 1 MeV for an isotropic flux is $\ll 10^{-5} \text{ cm}^{-2} \text{ sr}^{-1} \text{ s}^{-1} \text{ MeV}^{-1}$ (see Figure 4) compared with 1.4×10^{-2} for the electrons. Also, the proton range is less than that of electrons, so that, for instance, even the .17 cm thick cryostat window will stop all protons with incident energy less than 18 MeV [45].

4. Background Reduction Techniques

The sums of the calculated components shown by the solid lines in Figures 1 and 2, are seen to be generally consistent in both shape and magnitude with the observed continuum background spectra from the LEGS coaxial and planar detector arrays. Since the two detector configurations are quite different in terms of their fields of view, passive materials near the detectors, and detector volumes, the success of the calculations for both cases indicates that the background components are well understood. In this section, we study in more depth the nature of the different components, and suggest techniques for their reduction.

4.1 Passive Material and Shield Threshold

The aperture flux and shield leakage curves in Figures 1 and 2 are significantly higher and broader than one would calculate for a very low shield threshold and no passive material inside the shield. The extra background is due to photons that either scatter in the detector and are absorbed in the passive material or in the shield ($\Delta E < \text{shield threshold}$), or vice versa.

For the aperture flux, this increase is illustrated in Figure 7, where the ratio of the total aperture flux background to the contribution from unscattered photons is shown as a function of energy for the coaxial and planar detectors. The unscattered contribution is that due to photons that enter the aperture and are fully absorbed in the detectors. It can be simply calculated at a given energy by multiplying the downward gamma-ray flux (Figure 3) times the detector effective area (Figure 2 of Paciesas et al. [1]) times the aperture solid angle (Table 1) times an absorption factor (approximately equal to 1) to account for the instrument materials in the field of view (Section 2).

Two curves are shown in Figure 7 for the coaxial array, representing the extremes of uncertainty in the thickness of the inside walls of the shield (0.16 to 0.32 cm Al) and the shield threshold during the flight (100 to 200 keV). The coaxial curves are high at low energies because the unscattered spectrum falls off steeply toward lower energies due to the Ge deadlayer on the detectors, while the contribution from scattered photons is relatively constant in this energy range. The ratio reaches a minimum near 70 keV and then rises toward higher energies because of the increasing cross section for Compton scattering relative to photoelectric absorption.

For the planar array, the ratio in Figure 7 is approximately constant between 40 and 80 keV because the detectors have essentially no top dead-layer. The steep rise above 100 keV is caused by the increasing Compton-scattering cross section in this energy range in the iron collimator. The factor of ~ 5 increase in aperture flux background above 200 keV due to the massive Fe collimators close to the detectors in the planar array illustrates how significantly passive material inside the shield can enhance the background. The collimators are still a valuable feature of the LEGS planar configuration, however, since they do restrict the field of view and thereby decrease the background in the important energy range below 100 keV.

Table 3 itemizes the contribution of different passive materials inside the LEGS shield to the increase in aperture flux background in the 0.1 to 1.0 MeV range for the coaxial array. Out of the 71% total increase (thick shield housing, 200 keV shield threshold), 39% is due to single scatterings in a passive material, 13% is due to multiple scatterings, and 19% is due to events with energy (< 200 keV) deposited in the shield. We have not found a simple quantitative relationship between the increase in background caused by a particular material and the material parameters, such as mass, atomic number,

thickness, distance from detector, and covering factor. However, it is clear considering background increase per unit mass, that passive materials very near the detector, such as the Ge deadlayer and the Al detector housing, are particularly bad. The higher atomic number of the Ge also plays a role since the Ge deadlayer contribution is 2 1/2 times that of the Al detector housing, while the materials have similar masses and are both close to the detector.

Now turning to the shield leakage background, the increase due to the high shield threshold and passive material near the detectors is shown for the coaxial array in Figure 8. The curves labeled 1 and 3 are the total calculated shield leakage backgrounds for the two extreme cases of 0.32 cm thick shield housing walls and 200 keV shield threshold, and 0.16 cm thick walls and 100 keV threshold. The shield leakage curve used in Figure 1 is the geometric mean of these two curves, and is shown in Figure 8 by the dashed line, curve 2. The curve labeled "Unscattered Photons" represents the shield leakage background that would be obtained for an ideal instrument with only active Ge inside the shield and a 0 keV shield threshold. The most dramatic effect the passive material and shield threshold has on the background occurs at energies less than ~ 0.4 MeV. The unscattered component falls off steeply due to the rising absorption cross section of the shield, whereas the total background remains high. In this energy range, the background is caused almost entirely by higher energy photons that either scatter in the shield without triggering the threshold or scatter in passive material near the detectors. Curve 4 in Figure 8 shows the effect of the passive material by itself with a 0 keV shield threshold. At 1 MeV, the passive material inside the shield doubles the shield leakage background, and the 100 keV shield threshold contributes an additional 60%.

In order to further explore the effect of shield threshold on the shield

leakage background, we have performed Monte Carlo simulations for an instrument configuration that may be typical of new instruments. The instrument was assumed to have a 15.2 cm thick NaI shield surrounding (except for a 20° FWHM aperture hole) several coaxial n-type Ge detectors of dimension 7 cm diameter x 7 cm length**. No passive material was included inside the shield so that the effect of the shield threshold could be determined independently of other parameters. The calculation is for a flight at 3.5 g cm⁻² atmospheric depth over Palestine, Texas. The results are shown in Figure 9, where the ratio of the total shield leakage background to the leakage with a 0 keV threshold is plotted as a function of shield threshold for three energy bands. At energies greater than 2.5 MeV, where the shield leakage is by far the dominant background component, the increase in leakage due to the nonzero threshold is only in the few percent range for reasonable thresholds, but does approach 50% for high (~ 200 keV) thresholds. At lower energies the increase is much greater, but the total effect is not as important because the β^- component is also a significant fraction of the background. However, as will be discussed in Section 4.3, reduction techniques can be used in new instruments to substantially reducing the β^- component. In this case, the increase in the shield leakage background at lower energies can lead to a significant increase in the total background. Based on Figure 9, a shield threshold well below 50 keV is recommended.

The standard techniques for reducing the aperture flux and shield leakage backgrounds involve changing instrument parameters, such as aperture size and shield thickness. We have shown here that the background can also be

**For all calculations in this paper concerning coaxial detectors other than the LEGS coaxials, it is assumed that the cylindrical hole in the center of the detector for the inner contact is 1 cm in diameter and stops 1 cm below the top of the detector.

significantly reduced without such design changes by decreasing the amount of passive material inside the shield and by lowering the shield threshold as much as possible. At low and high energies where the aperture flux and shield leakage respectively dominate the background, a reduction in total background by more than a factor of 2 can be achieved, which means an improvement in sensitivity to spectral lines of more than 40% (see equation (6)).

Specific recommendations for reducing passive material and lowering the shield threshold are:

- 1) Use n-type coaxial Ge detectors with the reverse electrode configuration. For these detectors the thick (1-2 mm) Li-diffused deadlayer of Ge can be on the inner contact rather than the outer contact as is the case with the standard p-type detectors [46]. This reduces the volume of inactive Ge by a factor of ~ 9 assuming a coaxial detector of 7 cm diameter and 7 cm height.
- 2) Reduce the mass of the detector housing and cryostat to an absolute minimum, and use low-Z materials such as Al or, ideally, Be.
- 3) Replace the standard Cu coldfinger with an Al coldfinger, which gives the same thermal conductance for approximately half the mass.
- 4) Reduce passive materials in the aperture to an absolute minimum. This can be done by using an active collimator whenever possible. If a small field-of-view requirement dictates a passive collimator, the background produced by the collimator can be minimized by first using an active collimator, such as an aperture hole in the shield, to reduce the field of view to a few tens of degrees, and then placing the fine collimator at the end of the hole. The geometry factor for scattering into the detector is thereby much reduced compared with placing the passive collimator near the detectors. The inner housing walls of the aperture hole in the shield also contribute to the scattering background. This contribution can be eliminated by using thin Be

windows on either side of the hole, so that the inner housing wall is eliminated altogether. The Be will be directly in the field of view, but the attenuation of the incoming photon beam is extremely small; for instance, if windows of 0.05 cm thickness are used, the attenuation at 20 keV for two windows is only 4%.

5) Use NaI scintillator for the shield in order to set as low a shield threshold as possible. Experience has shown that setting a low threshold, below 50 keV, in a large-volume NaI shield at balloon altitudes, without producing an unacceptable deadtime, is an extremely difficult challenge. Of the three commonly used scintillators (NaI, CsI, BGO), NaI has the highest light output per unit energy loss in the shield (relative numbers 1.0, 0.85, 0.13) and the shortest light decay constant (0.23 μ s, 0.63 μ s, 0.3 μ s). It is therefore even more difficult to set low thresholds in the other two scintillators than in NaI. There are many other important criteria that enter into the decision of what scintillator to use for a shield (such as cost, availability, instrument geometry, and weight), but strictly from the standpoint of minimizing shield leakage background by setting as low a shield threshold as possible, NaI is the scintillator of choice. Experience has also shown that light collection uniformity from the scintillator is a critical parameter in actually achieving a low threshold during a flight.

All of the above recommendations are being incorporated into a new instrument that is currently being built as a collaboration among groups at Bell Laboratories, Goddard Space Flight Center, and Sandia National Laboratories, Albuquerque. The total mass of passive material inside the shield for this instrument is \sim 3.5 kg (almost all of which is Al), which is a similar mass to the \sim 5 kg for the LEGS coaxial array. However, the new instrument is designed for seven Ge detectors, each 7 cm in diameter by 7 cm

in length. Therefore, the total passive mass per unit volume of Ge is $\sim 2 \text{ g cm}^{-3}$ which is an order of magnitude less than the $\sim 20 \text{ g cm}^{-3}$ for LEGS.

In addition to decreasing the continuum background, reducing the passive material inside the shield also results in a decrease in the intensity of the background line at 511 keV. Part of this background is due to positrons which are created in the passive material via pair-production and nuclear interactions, and then annihilate producing two 511-keV photons. This energy is of particular interest for present and future gamma-ray spectrometers since positrons can also be produced in astrophysical sources.

4.2 Aperture Size

In the energy range from 30 to 100 keV where the aperture flux dominates the background, the most straightforward approach to reducing the background is to decrease the field of view of the instrument. The effect can be seen by comparing the aperture flux for the LEGS wide field-of-view coaxial array with the narrow field-of-view planar array. Since the relevant quantity to compare for front-incident low-energy photons is the background per unit detector effective area, we normalize the backgrounds in Figures 1 and 2 by the coaxial and planar effective areas in Figure 2 of Pacieras et al. [1]. At 100 keV, the coaxial aperture flux background per unit detector effective area is $0.33 \text{ cnts s}^{-1} \text{ MeV}^{-1} \text{ cm}^{-2}$ compared with $0.067 \text{ cnts s}^{-1} \text{ MeV}^{-1} \text{ cm}^{-2}$ for the planar array. The planar array has 5 times less aperture flux background at this energy, which is consistent with the aperture solid angles of the two configurations (0.08 sr - coaxials, 0.015 sr - planars; see Table 1). Below 100 keV, the shape of the coaxial and planar aperture flux backgrounds in Figures 1 and 2 are quite different from one another. The planar background has a maximum at 35 keV due to the peak in the incident gamma-ray spectrum at

this energy (Figure 3), whereas the coaxial background has a maximum at a 85 keV due to the Ge deadlayer on top of the detectors.

An interesting question that can be answered with the present calculation results is: How small an aperture is required to reduce the aperture flux background to the level of the elastic neutron scattering background in new instruments? The comparison will be done at 40 keV and at an atmospheric depth of 3.5 g cm^{-2} over Palestine, Texas. For an instrument with a 15.2 cm thick NaI shield, the elastic neutron scattering background is $5.0 \times 10^{-2} \text{ cnts s}^{-1} \text{ MeV}^{-1} \text{ cm}^{-3}$ at 40 keV. The incident photon flux at this energy is $17 \text{ photons cm}^{-2} \text{ sr}^{-1} \text{ s}^{-1} \text{ MeV}^{-1}$ or $5.2 \times 10^{-3} \text{ photons cm}^{-2} \text{ (square degree)}^{-1} \text{ s}^{-1} \text{ MeV}^{-1}$, and the detector efficiency is near unity. Therefore, we find that, for an instrument with an aperture solid angle of Ω , detectors of thickness d , and no deadlayer on the detectors (i.e., either a planar detector or an n-type coaxial detector), the aperture flux background is equal to the elastic neutron scattering background at 40 keV if

$$\frac{\Omega}{d} \approx 10 \quad (\text{square degrees}) \text{ cm}^{-1}. \quad (5)$$

If the aperture size is being chosen to minimize the instrument background, then equation (5) gives an approximate lower limit that need be considered for Ω ; reducing Ω much more gives diminishing returns since the elastic neutron scattering then dominates the background.

For a planar detector of 1 cm thickness or a segmented coaxial detector (see Section 4.3) with top segment of 1 cm thickness, and assuming a square field of view, equation (5) recommends a field of view of size approximately $3^\circ \times 3^\circ$. For a 5 cm, unsegmented detector, the field of view need not be much smaller than $7^\circ \times 7^\circ$ if background reduction is the goal.

4.3 Detector Segmentation

The understanding of the nature and relative intensities of the various background components gained with the present background study, has led to a new detector concept that promises to improve the sensitivity of future gamma-ray spectrometers. In this section, we describe the detector and calculate its performance as a function of various detector and instrument parameters.

At low energies, the background in future instruments with narrow fields of view will be largely detector-volume dependent while the signal from incident low-energy gamma rays on the top surface of the detector is area dependent. The one background component that is not volume dependent is the aperture flux, but for narrow field-of-view instruments (unlike LEGS) this component is small. This is illustrated in Figure 10a which shows the calculated background components for an instrument with a $3^\circ \times 3^\circ$ field of view, coaxial n-type germanium detectors of size 7 cm diameter by 7 cm length, a 15.2 cm thick NaI shield with threshold set at 20 keV, and 500 g per detector of passive Al inside the shield. As mentioned in Section 4.1, n-type Ge detectors have the thin contact on the outside surface, thereby eliminating the thick deadlayer on the top of the detector and allowing low-energy photons (10 to 100 keV) to be detected with essentially no attenuation. Since the background below 100 keV in Figure 10a is dominated by the volume-dependent elastic neutron scattering component, the desire is for a thin large-area detector in this energy range. At high energies, however, both the background and the signal are volume dependent, so that the instrument sensitivity increases with increasing detector volume. With the LEGS instrument, these two opposing conditions were met by having two detector arrays - the planar array for low-energy observations and the coaxial array for high-energy observations.

The new idea is to have a single large coaxial detector with its outer side contact segmented into several horizontal rings. Although the detector is maintained as a single device, the use of the signals from the segmented contact give it characteristics similar to those of a stack of planar detectors. The high-resolution signal is still obtained from the unsegmented inner contact, while the information from the segmented outer contact is stored as tags for each event, to be used during data analysis. For the present discussion of the low-energy response, the relevant segment is the top one. If only those events which have signal in the top segment and none in the lower segments are used at low energies, the background is reduced by approximately the ratio of the top segment volume to the total detector volume. At the same time, the efficiency for detecting low-energy gamma rays incident through the aperture is essentially unchanged. The sensitivity in this energy range is therefore improved, as will be discussed more quantitatively below. The background reduction for a 1 cm thick top segment is illustrated in Figure 10b. The background per unit volume of Ge for this top segment mode is seen to be roughly the same intensity as the volume-normalized all-events background in panel (a). Therefore, since the volume of the top segment is a factor of ~ 7 smaller than the volume of the whole detector, the background per detector is significantly reduced.

At higher energies, the segmented detector can be used in a different mode to reduce the background. The idea here is that between 150 keV and 1 MeV the background is dominated by the localized β^- decays (Figure 10a), which are predominately decays to the ground state of the daughter nuclide. As discussed in Section 3, the signal for each event is caused by the energy loss of the β^- electron, and is therefore produced in a very small region ($\lesssim 1$ mm) of the detector due to the short range of electrons at these energies. The

elastic neutron scattering background, which dominates below 100 keV and is important up to 300 keV, is also a localized interaction with ionization limited to an extremely small region for each event. In contrast, the incident gamma rays in the 150 keV to 1 MeV range interact predominantly via Compton scatterings, which produce ionization at more than one site in the detector. Hence, if only those events which have signal in more than one segment are accepted, the background is substantially reduced while the gamma-ray detection efficiency remains high. This concept is illustrated in Figure 11.

The background for multiple-segment events is shown in Figure 10c. The plot is for detectors with 7 segments, each 1 cm thick, assumed to have no dead region between segment boundaries and to have very low segment thresholds (any energy deposition causes the segment to be included in the coincidence). With the multiple-segment requirement, the elastic neutron scattering component is eliminated from the background, and the aperture flux cuts off sharply below 100 keV since events with lower energies are almost all top-segment-only events. The localized β^- decays are reduced by more than an order of magnitude, but are not entirely eliminated because some of the β^- electrons cross segment boundaries. To determine the magnitude of this effect, a Monte Carlo program was written that propagates electrons in a segment. It was assumed that all electrons at a given energy have the same range, which was taken to be their extrapolated range (see footnote in Section 3.3). Since the extrapolated range is at the upper end of the range distribution for actual electrons, this assumption results in an overestimate of the number of localized β^- decays that contribute to the multiple-segment background. The nonlocalized β^- decays are an important component of the multiple-segment background, although their intensity is less than in the all-events mode due to the fact that many of the prompt gamma-rays are absorbed in

the same segment as the β^- -decay event. The shield leakage component is also less intense and cuts off more steeply toward lower energies than in the all-events mode, but is the dominant component at almost all energies. The total background in the multiple-segment mode is seen to be reduced from the all-events mode by more than an order of magnitude between 150 and 500 keV and a factor of five at 1 MeV.

The idea of segmenting the contact on Ge detectors for medical imaging purposes [47,48] and for some limited background rejection applications [49-51] has been around for many years. Also, the concepts of using thin, large-area detectors to minimize background in the hard X-ray energy range and Compton telescopes to minimize background in the MeV energy range are not new. What is new in the detector concepts presented recently by Gehrels et al. [13], Roth et al. [52], and Varnell et al. [53], and analyzed in detail here, is the idea of using segmentation to reduce both the low-energy and medium-energy backgrounds in a single Ge detector.

The relevant quantity for comparing the performance of a segmented detector with that of an unsegmented detector is not the background level, but rather the instrument sensitivity for detection of lines in a source spectrum. The sensitivity is the minimum flux in a spectral line that can be detected at a given significance level in a given amount of time, so that lowering the sensitivity represents an improvement. The sensitivity, S , is given by

$$S = \frac{2 k (n V \Delta E B f t)^{1/2}}{\exp(-\mu x) n A \epsilon f t G} \quad \text{photons cm}^{-2} \text{ s}^{-1} \quad (6)$$

where k is the significance level of the line search (# of σ), n is the number of detectors of volume V (cm^3) and area A (cm^2), ΔE is the energy interval

(MeV) searched, B is the background (cnts s^{-1} MeV $^{-1}$ cm $^{-3}$) in that interval, f is the livetime fraction during the observation, t is the total observing time (s) assumed to be equally divided into source and background observations, μ is the attenuation factor (cm 2 g $^{-1}$) in air, x is the atmospheric depth (g cm $^{-2}$) along the line of sight of the telescope pointing direction, ϵ is the full-energy-peak gamma-ray detection efficiency, and G is the fraction of the line flux that is contained in the interval ΔE given the instrumental resolution. It was assumed in the derivation of the equation that the observation is background limited and that the number of background counts in ΔE is much greater than 1 so that Gaussian statistics apply. In the analysis below, we use the following values: $k=3$, $n=7$, $\Delta E=4 \times 10^{-3}$ MeV which is close to the optimum energy interval for a narrow-line search [3] given the ~ 3 keV energy resolution expected for the new detectors, $G=0.88$ based on this choice of ΔE , $x = 3.5$ g cm $^{-2}$, $f=0.9$, and $t=2.88 \times 10^4$ s (8 hours).

An interesting aspect of both the top-segment and multiple-segment modes is that not all events are used when these modes are employed. A small additional improvement in sensitivity can therefore be obtained by also including in the analysis the leftover events, albeit with their higher background level and lower gamma-ray efficiencies. For example, in the case of the multiple-segment mode, single-segment events can also be analyzed and the two sensitivities combined in quadrature. Denoting the efficiency, background, and volume for the primary mode as ϵ_1 , B_1 , and V_1 , and for the remaining events as ϵ_2 , B_2 , and V_2 , and using the above values for the various parameters in equation (6), the sensitivity becomes

$$S = \frac{1.01 \times 10^{-3}}{\exp(-\mu \cdot 3.5) A} \left(\frac{\epsilon_1^2}{V_1 B_1} + \frac{\epsilon_2^2}{V_2 B_2} \right)^{-1/2} . \quad (7)$$

For the all-events mode, there are no leftover events and the second term does not apply ($\epsilon_2 = 0$).

Figure 12 shows the efficiencies for the three analysis modes obtained with the Monte Carlo code. Using this data, the background data in Figure 10, and equation (7), we have calculated the narrow-line sensitivity for the three segment coincidence modes assuming an instrument configuration with 7 detectors of size 7 cm diameter and 7 cm height, each with its cathode divided into 7 segments, and surrounded by a 15.2 cm thick NaI shield. The results are shown in Figure 13. Since these sensitivity curves are based on the calculated continuum backgrounds not including the background lines, they do not apply at the energies of the strong background lines, such as 23, 67, 140, 198, 511, 844, 1369, and 1461 keV. The solid line gives the all-events sensitivity which would be obtained with unsegmented detectors, and is approximately a factor of 4 to 6 better than existing instruments such as LEGS. The dashed lines show the improvement that can be obtained with a segmented detector using the top-segment and multiple-segment modes, and the upper panel gives the ratios of the all-events sensitivity to the sensitivities for the segmented modes. The conclusion is that the sensitivity can be improved by approximately a factor of 2 between 20 and 700 keV by using a segmented detector. The significance of a factor of 2 gain in sensitivity is best appreciated by considering that the number of unsegmented detectors in an instrument would have to be increased by a factor of 4 to achieve a similar gain. In the next several paragraphs, we explore the dependence of the sensitivity improvement on the number of segments per detector, the detector size, and the shield parameters.

Figure 14 shows the sensitivity improvement factor at three different energies for segmented detectors (relative to unsegmented detectors) as a

function of the number of segments equally dividing the outer side contact of the detector. Panel (a) is for 30 keV where the top-segment mode applies, and therefore pertains only to the thickness of the top segment. The improvement at this energy is a strong function of segment thickness and only begins leveling off for extremely thin top segments in the 1 to 2 mm range. The sensitivity gain for these thicknesses is more than a factor of 3. Of course, at slightly higher energies, the incident gamma rays penetrate deeper into the detector and the improvement curves level off at larger top-segment thicknesses. For instance, already at 40 keV the curve levels off closer to a 1 cm segment thickness, as was predicted by equation (5).

Panels (b) and (c) of Figure 14 show the improvements at 0.2 and 1 MeV for the multiple-segment mode. In these cases, only a small gain is achieved by having more than approximately 10 segments per detector. Toward smaller numbers of segments, the improvement at 0.2 MeV falls off steeply below 4 segments. An interesting special case shown by '+'s in the figure is a 2-segment detector with unequal segment thicknesses, 1 cm on top and 6 cm on the bottom. At 0.2 MeV, this detector performs approximately as well as the 7-segment detector, although at 1 MeV its relative performance is down. The reason it does so much better at 0.2 MeV than the detector with 2 equal segments is that, for top-incident gamma rays at this energy, a very common event is one that interacts via a Compton scattering near the top of the detector with the scattered photon traveling on the order of a centimeter before being photoabsorbed. These are included as valid multiple-segment events for the 1 cm/6 cm detector but not for the equal-segment detector. At 1 MeV, the scatterings occur typically deeper in the detector, and the relative performance of the 1 cm/6 cm detector is not as good. Since any multisegment detector with a 1 cm top segment gives the same segment

information as the 1 cm/6 cm detector, plus additional information, it is possible to devise analysis schemes for a multisegment detector that are more complicated than the multiple-segment mode and that take advantage of the specific interaction mechanisms at various energies. For instance, at 0.2 MeV the multiple-segment events that include the top segment can be analyzed separately from those that do not, and the sensitivities combined as in equation (7). The improvement factor for a 7-segment detector increases from 1.9 to 2.2 using this technique at 0.2 MeV, as shown by the open circle in the figure.

There are undoubtedly other segment coincidence conditions that give even larger sensitivity gains in specific energy ranges. The advantage of recording all events during the observations, regardless of segment coincidence, is that the optimum mode in each energy range can be chosen during the data analysis to give the best sensitivity. The larger the number of segments, the more possibilities are available, so that a trade-off exists between complexity in data analysis and instrumentation versus possible sensitivity gains. Figure 14 indicates that diminishing returns occur for detectors with more than 10 segments. The figure also shows the benefits at low energies of having as thin a top segment as possible.

In Figure 15, we show the effect of detector size on the sensitivity improvement obtainable with a segmented detector. A constant segment thickness of 1 cm was assumed in the calculation, so that the number of segments per detector increases from 5 for the 5 cm detector to 8 for the 8 cm detector. At 1 MeV, the sensitivity improvement is fairly flat, indicating on the one hand that segmentation is a useful technique even if one is using only 5 cm detectors, but on the other hand that the improvement factor will not increase much as one obtains larger detectors. At 0.2 MeV, the difference

between small and large detectors is larger, but the general conclusions are the same.

In Figure 16 the effect on the sensitivity improvement of changing the shield thickness and threshold is shown. The shield thickness is seen to be a critical parameter for detector segmentation. This is not surprising since the background in the multiple-segment mode is dominated by the shield leakage component (see Figure 10c). For a 10 cm thick NaI shield, detector segmentation is probably not worthwhile for achieving sensitivity improvement in the multiple-segment mode. Segmentation becomes useful for shields thicker than ~ 12 cm, and is a powerful technique for shields in the 15 to 20 cm thickness range. The shield threshold level is also an important parameter, as can be seen in panels (c) and (d). The benefit of segmented detectors is significantly decreased for threshold levels over ~ 100 keV.

5. Conclusions

The necessary analytical tools and data on interaction cross sections and atmospheric radiation fluxes are now available for performing detailed calculations of the background observed by gamma-ray spectrometers flown in the upper atmosphere. For spectrometers with Ge detectors and thick active shields, the components of the continuum background are: 1) elastic neutron scattering which is due to atmospheric neutrons that penetrate the shield and scatter elastically on the Ge nuclei in the detector, and is important at low energies ($\lesssim 100$ keV); 2) aperture flux which is due to atmospheric and cosmic gamma rays that enter the aperture of the instrument and which can be important at low energies ($\lesssim 100$ keV) depending on the instrument field of view; 3) β^- decays which are due to protons and neutrons produced in the atmosphere and in the shield that interact with the Ge nuclei to produce β^- -

unstable nuclides, and are important between 100 keV and 1 MeV; and 4) shield leakage which is due to the small fraction of atmospheric gamma rays that penetrate the shield without depositing more energy in it than the shield threshold, and is the dominant component at high energies ($\gtrsim 1$ MeV).

The detailed study of the background components presented in this paper has led to a better understanding of their nature and to several specific recommended techniques for reducing the background in future instruments. In present instruments such as the Goddard LEGS instrument, the aperture flux and shield leakage backgrounds are increased by factors of $\gtrsim 2$ by passive material inside the shield (such as the Ge deadlayer on the detectors, the detector coldfinger, the detector housings and cryostat, passive collimators in the aperture, and housings on the shield) and by relatively high ($\gtrsim 100$ keV) thresholds in the shield. Concerning the passive material, recommendations include using n-type Ge detectors with the thin outer deadlayer, building detector housings and cryostats with the minimum possible low-Z material, replacing the standard Cu coldfinger with an Al coldfinger, and using active collimators when possible. To obtain as low a shield threshold as possible, NaI is the scintillator of choice and light collection uniformity from the scintillator is a critical parameter.

A new type of detector made from n-type Ge with its outer contact segmented into horizontal rings can be used to significantly reduce the background in future spectrometers. By using different segment coincidence modes in different energy ranges, the instrument's sensitivity to spectral lines can be improved at both low and medium energies. At low energies, the dominant background component in future narrow field-of-view instruments will be elastic neutron scattering, which occurs uniformly throughout the detector. Incident low-energy gamma rays, on the other hand, interact

predominantly in the top region of the detector, so that by analyzing only top-segment events at low energies the signal to background ratio is improved. For instance, for detectors of size 7 cm diameter by 7 cm height with a 1 cm thick top segment, inside a 15.2 cm thick NaI shield and with a $3^\circ \times 3^\circ$ field of view, the sensitivity is improved by a factor of ~ 2 between 20 and 100 keV.

At medium energies (100 keV to 1 MeV), background for the above instrument configuration is dominated by the β^- -decay component, which our calculations show is made up almost entirely of decays to the ground state of the daughter nuclides. Since no prompt gamma rays are emitted, and since the range of the β^- electron is small at these energies, ionization in the detector is confined to small localized regions. On the other hand, incident gamma rays at these energies interact predominantly via Compton scattering that deposit ionization in more than one region of the detector. Therefore the signal to background ratio is increased by accepting only multiple-segment events. For a 7-segment detector, this technique gives a sensitivity improvement of a factor of 1.5 to 2 between 150 keV and 1 MeV. The sensitivity improvement that can be obtained in this multiple-segment mode depends critically on shield thickness and threshold. For example, concerning shield thickness, the improvement factor at 0.2 MeV is only 1.3 for a 12 cm thick NaI shield, but increases to > 2 for > 15 cm.

Acknowledgements

I greatly appreciate the advice and support of B. Teegarden who suggested this study and contributed many of the ideas. Thanks are also due to M. Leventhal, C. MacCallum, W. Paciesas, and J. Tueller for useful discussions. R. Howerton compiled and made available to me new cross section data on Ge for which I am grateful. An important tool in this study that I very much appreciated was a computer code provided by R. Silberberg and C. Tsao which conveniently generated their most recent proton interaction cross sections. I thank R. Kinzer for sending me data from the NRL balloon instrument, extending their gamma-ray spectrum to lower energies than had been published. I am grateful to E. Schronce for typing the manuscript of this paper.

Appendix

For each interaction contributing to the β^- -decay background, three different nuclides are involved. The first, which will be labeled "i", is the Ge isotope that the incident neutron or proton interacts with. The second, labeled "j", is the product nuclide created in the interaction, which in turn beta decays to the daughter nuclide, labeled "k". The daughter nuclide may be produced in an excited state that, in most cases, decays promptly to the ground state emitting one or more gamma rays. The equation for calculating the count rate per unit volume of Ge for each interaction and decay is

$$R_{ijk} = a_i b_j d_{jk} \epsilon_k (1 - 2^{-t/\tau_j}) \frac{10^{-24} \rho N_A}{w} \int_0^{\infty} \sigma_{ij} j dE \quad \text{cnts s}^{-1} \text{ cm}^{-3} \quad (8)$$

where a_i is the abundance fraction (atoms) of the i^{th} isotope of Ge, b_j is the β^- branching fraction of the interaction product, d_{jk} is the fraction of the β^- decays that go to the nuclear state of interest of the daughter nuclide, ϵ_k is the probability that the prompt gamma rays produced in the decay do not escape the detector and cause a shield veto ($\epsilon_k \equiv 1$ for ground-state decays), t is the time since the interactions started which we take to be the time since the instrument ascended through the Pfozter maximum in the proton and neutron fluxes ($t = 6$ hours in this analysis), τ_j is the β^- -decay half-life of the interaction product, 10^{-24} is the number of cm^2 per barn, ρ is the density of the target material, N_A is 6.02×10^{23} atoms mole^{-1} , w is the atomic weight of the target material, σ_{ij} is the cross section in barns for a neutron or proton incident on a nucleus of the i^{th} isotope of Ge to produce the j^{th} β^- -unstable product, and j is the neutron or proton flux at the detector in units of $\text{cm}^{-2} \text{ s}^{-1} \text{ MeV}^{-1}$ (see Figure 4).

The rates for all possible interactions of neutrons or protons on the

five stable isotopes of Ge to produce β^- -unstable nuclides were either calculated or estimated with enough accuracy to justify neglecting them. There are five isotopes of Ge, two types of incident particle, over 100 possible final states that are β^- unstable [35], and in many cases more than one decay mode, so that well over 1000 rates had to be calculated or estimated. In Table 4, the relevant data for approximately 700 of these rates are listed. The interactions have been divided into two types: the simple interactions which are defined as (n,γ) , (n,p) , $(n,2p)$, (n,np) , $(n,2n)$, (n,α) , (p,γ) , (p,n) , $(p,2n)$, (p,np) , $(p,2p)$, and (p,α) ; and the complex interactions (sometimes called spallation interactions) which include all others. All simple interactions producing β^- -unstable nuclides are listed in the table, with the exception of the $(n,2p)$ and (p,γ) interactions whose cross sections were not available. The reason we could not find cross sections for these two interactions is, almost certainly, that the cross sections are extremely small. For instance, for Mn where the cross sections are available, the value for $(n,2p)$ at 15 MeV is $\leq .3$ millibarn [54] and for (p,γ) at 10 MeV is .1 millibarn [55], compared with more typical values for the other interactions of 10 to 100 millibarn. The decays in the table with rates greater than roughly $1.5 \times 10^{-6} \text{ s}^{-1} \text{ cm}^{-3}$ are numbered, whereas those with smaller rates are labeled "s" for small. This cutoff is three orders of magnitude smaller than the highest rate of $3.9 \times 10^{-3} \text{ s}^{-1} \text{ cm}^{-3}$ for the ground-state decay of ^{75}Ge produced by $^{74}\text{Ge}(n,\gamma)^{75}\text{Ge}$. The interactions labeled as $X(\beta^-)Y$ are for the two-step process where a β^- -unstable nuclide is produced by the decay of another unstable nuclide.

For the complex interactions in Table 4, the rates for neutrons and protons incident on all five Ge isotopes to yield a given product nuclide were summed together and listed under that nuclide. These listings are therefore

typically each the sum of 10 rates. In general, cross sections were not available for the neutron-induced complex interactions, so we used proton cross sections in these cases. This should not introduce large errors in the results since the neutron and proton cross sections are similar at the high energies required to produce the complex interactions.

For each decay, Table 4 indicates whether it is localized or nonlocalized (see Section 3.3), and gives the β^- half-life and branching percentage, the decay mode and decay forbiddenness, the β^- endpoint energy, the rate, and the cross-section reference. All of the decay data are from the Table of Isotopes [35]. Only those nonlocalized decays accompanied by one prompt gamma ray are included in the decay mode listings (except in a few cases where a second gamma ray has very low energy). It was assumed that, for multiple gamma-ray decays, the probability of having radiation escape the detector and interact in the shield is high. For decays with single prompt gamma rays, the factor ϵ_k in equation (8) was assumed to be the probability that the gamma ray is totally absorbed in the detector, as discussed in Section 3.3. The value of this probability was determined with a Monte Carlo program, and is shown as a function of gamma-ray energy in Figure 17 for two different detector sizes. The absorption efficiencies for the LEGS coaxial detectors were used in calculating the rates listed in Table 4.

Given the rates, the next step is to determine the β^- energy spectrum for each decay, and then to sum the spectra into final localized and nonlocalized background spectra such as those shown in Figures 1, 2 and 10. The formula for the β^- energy spectrum is given by Behrens and Szybisz [36] as

$$N(E) \propto N(W) \propto p W (W_0 - W)^2 F(Z, W) C(W) \quad (9)$$

where E is the kinetic energy of the β^- electron, $W = E/mc^2 + 1$ is the total electron energy in units of mc^2 , $mc^2 = 0.511$ MeV is the electron rest mass, $N(E)$ and $N(W)$ are the number of decays per unit time per unit kinetic energy and total energy respectively, $p = (W^2 - 1)^{1/2}$ is the electron momentum in units of mc , $W_0 = E_0/mc^2 + 1$ is the endpoint total energy in units of mc^2 , E_0 is the endpoint kinetic energy (Table 4), $F(Z, W)$ is the Fermi function, Z is the atomic number of the daughter nucleus, and $C(W)$ is a correction factor whose form depends on the forbiddenness of the decay (Table 4) and whose numerical parameters are given by Behrens and Szybisz. We obtained values for the Fermi function and other functions needed for calculating $C(W)$ from the Landolt-Börnstein data tables [56]. The spectra were normalized to have integrals equal to the rates in Table 4. For those decays with a prompt gamma ray, the β^- spectrum was offset by the gamma-ray energy since both signals are collected in the detector.

The β^- decay spectra calculated using equation (9) and the data in Table 4 are shown in Figure 18 for all the decays that are numbered in the table. The figure is divided into three panels in order to minimize confusion among the spectra. The localized decays have short-dashed curves, and the nonlocalized decays have long-dashed curves. The solid line is the sum of the localized decays. For the localized decays, the dominant interaction is ${}^{74}\text{Ge}(n, \gamma){}^{75}\text{Ge}$ followed by the complex interactions producing ${}^{70}\text{Ga}$ and ${}^{69}\text{Zn}$. Although all other decays fall considerably below these three, there are a large number of them, and their contribution makes up $\sim 20\%$ of the total below 60 keV and over half of the total above 1 MeV. For the nonlocalized decays, ${}^{74}\text{Ge}(n, \gamma){}^{75}\text{Ge}$ is by far the dominant interaction.

References

- [1] W. Paciesas, R. Baker, D. Boclet, S. Brown, T. Cline, H. Costlow, Ph. Durouchoux, C. Ehrmann, N. Gehrels, J. M. Hameury, R. Haymes, B. Teegarden, and J. Tueller, *Nucl. Instr. and Meth.* 215 (1983) 261.
- [2] E. A. Womack and J. W. Overbeck, *J. Geophys. Res.* 75 (1970) 1811.
- [3] A. S. Jacobson, R. J. Bishop, G. W. Culp, L. Jung, W. A. Mahoney, and J. B. Willett, *Nucl. Instr. and Meth.* 127 (1975) 115.
- [4] W. L. Imhof, G. H. Nakano, and J. B. Reagan, *J. Geophys. Res.* 81 (1976) 2835.
- [5] M. Leventhal, C. MacCallum, and A. Watts, *Astrophys. J.* 216 (1977) 491.
- [6] W. A. Mahoney, J. C. Ling, J. B. Willett, and A. S. Jacobson, in Gamma Ray Spectroscopy in Astrophysics, eds. T. L. Cline and R. Ramaty, NASA TM-79619 (1978) 462.
- [7] F. Albernhe, D. Boclet, J. P. Chabaud, J. Claisse, Ph. Durouchoux, P. Frabel, E. Olivier, J. M. da Costa, P. Pagnier, R. Rocchia, and G. Vedrenne, *Nucl. Instr. and Meth.* 155 (1978) 171.
- [8] L. E. Peterson, R. M. Pelling, and J. L. Matteson, *Space Sci. Rev.* 13 (1972) 320.
- [9] J. C. Ling, Thesis, Univ. of California, San Diego (1974).
- [10] J. L. Matteson, P. L. Nolan, W. S. Paciesas, and R. M. Pelling, *Space Sci. Instr.* 3 (1977) 491.

- [11] G. R. Ricker, J. V. Vallergera, and D. R. Wood, *Nucl. Instr. and Meth.* 213 (1983) 133.
- [12] J. C. Ling, W. A. Mahoney, J. B. Willett, and A. S. Jacobson, *J. Geophys. Res.* 82 (1977) 1463.
- [13] N. Gehrels, T. L. Cline, B. J. Teegarden, J. Tueller, M. Leventhal, C. J. MacCallum, P. V. Hewka, and P. Ryge, *IEEE Trans. Nucl. Sci.* NS-31, No. 1 (1984) 307.
- [14] R. L. Kinzer, private communication (1983).
- [15] R. L. Kinzer, W. N. Johnson, and J. D. Kurfess, *Astrophys. J.* 222 (1978) 370.
- [16] V. Schönfelder, F. Graml, and F.-P. Penningsfeld, *Astrophys. J.* 240 (1980) 350.
- [17] J. A. Lockwood, L. Hsieh, L. Friling, C. Chen, and D. Swartz, *J. Geophys. Res.* 84 (1979) 1402.
- [18] J. C. Ling, *J. Geophys. Res.* 80 (1975) 3241.
- [19] J. M. Ryan, B. Dayton, S. H. Moon, R. B. Wilson, A. D. Zych, and R. S. White, *J. Geophys. Res.* 82 (1977) 3593.
- [20] R. S. White, B. Dayton, S. H. Moon, J. M. Ryan, R. B. Wilson, and A. D. Zych, *Astrophys. J.* 218 (1977) 920.
- [21] V. Schönfelder, U. Graser, and J. Daugherty, *Astrophys. J.* 217 (1977) 306.
- [22] R. D. Evans, The Atomic Nucleus, McGraw-Hill, New York (1955) 625.

- [23] K. F. Koral and A. J. Cohen, NASA TN D-2909 (1965).
- [24] R. L. Kelly et al., Rev. Mod. Phys. 52, No. 2, Part II (1980) S1.
- [25] T. W. Armstrong, K. C. Chandler, and J. Barish, J. Geophys. Res. 78 (1973) 2715.
- [26] B. Rossi, High-Energy Particles, Prentice-Hall, Englewood Cliffs, NJ (1952) 486.
- [27] F. B. McDonald and W. R. Webber, Phys. Rev. 115 (1959) 194.
- [28] W. R. Webber and J. A. Lezniak, Astrophys. and Space Sci. 30 (1974) 361.
- [29] W. E. Alley and R. M. Lessler, Lawrence Livermore Lab. Report No. UCRL-50484, rev. 1 (1972).
- [30] Handbook on Nuclear Activation Cross-Sections, Intl. Atomic Energy Agency Tech. Report Series No. 156, Vienna (1974).
- [31] D. I. Garber and R. R. Kinsey, Brookhaven National Lab. Report No. 325, 3rd ed., vol. II (1976).
- [32] R. J. Howerton, D. E. Dye, and S. T. Perkins, Lawrence Livermore Lab. Report No. UCRL-50400, vol. 18, rev. 1 (1982).
- [33] R. Silberberg and C. H. Tsao, Astrophys. J. Suppl. 25 (1973) 315.
- [34] _____, Astrophys. J. Suppl. 25 (1973) 335.
- [35] Table of Isotopes, eds. C. M. Lederer and V. S. Shirley, 7th ed., Wiley, New York (1978).

- [36] H. Behrens and L. Szybisz, Shapes of Beta Spectra, Phys. Data 6-1 (1976).
- [37] G. F. Knoll, Radiation Detection and Measurement, Wiley, New York (1979) 571.
- [38] D. I. Garber, L. G. Strömberg, M. D. Goldberg, D. E. Cullen, and V. M. May, Brookhaven National Lab. Report No. 400, 3rd. ed., vol. I and II (1970).
- [39] J. W. Corbett, Electron Radiation Damage in Semiconductors and Metals, Academic Press, New York (1966) 135.
- [40] J. Lindhard, V. Nielsen, M. Scharff, and P. V. Thomsen, Danske Vid. Selskab, Mat.-fys. Medd. 33, No. 10 (1963).
- [41] M. T. Robinson, in Nuclear Fusion Reactors, eds. J. L. Hall and J. H. C. Maple, British Nucl. Energy Soc., London (1970) 364.
- [42] R. R. Daniel and S. A. Stephens, Rev. Geophys. and Space Phys. 12 (1974) 233.
- [43] J. M. Lavigne, M. Niel, G. Vedrenne, B. Arginier, E. Bonfand, B. Parlier, and K. R. Rao, Astrophys. J. 261 (1982) 720.
- [44] G. Fulks and P. Meyer, J. Geophys. 40 (1974) 751.
- [45] J. F. Janni, Air Force Weapons Lab. Tech. Report No. AFWL-TR-65-150, Kirtland Air Force Base, New Mexico (1966).
- [46] T. W. Raudorf, R. C. Trammell, and L. S. Darken, Jr., IEEE Trans. Nucl. Sci. NS-26, No. 1 (1979) 297.

- [47] R. P. Parker, E. M. Gunnerson, J. L. Wankling, and R. Ellis, *Medical Radioisotope Scintigraphy* 1, IAEA (1969) 71.
- [48] M. G. Strauss and I. S. Sherman, *IEEE Trans. Nucl. Sci.* NS-19, No. 3 (1972) 219.
- [49] C. R. Gruhn, J. V. Kane, W. H. Kelley, T. Kuo, and G. Berzins, *Nucl. Instr. and Meth.* 54 (1967) 268.
- [50] J. M. Palms, R. E. Wood, and O. H. Puckett, *IEEE Trans. Nucl. Sci.* NS-15, No. 3 (1968) 397.
- [51] A. R. Sayres and J. A. Baicker, *IEEE Trans. Nucl. Sci.* NS-15, No. 3 (1968) 393.
- [52] J. Roth, J. H. Primbsch, and R. P. Lin, *IEEE Trans. Nucl. Sci.* NS-31, No. 1. (1984) 367.
- [53] L. S. Varnell, J. C. Ling, W. A. Mahoney, A. S. Jacobson, R. H. Pehl, F. S. Goulding, D. A. Landis, P. N. Luke, and N. W. Madden, *IEEE Trans. Nucl. Sci.* NS-31, No. 1 (1984) 300.
- [54] E. T. Bramlitt and R. W. Fink, *Phys. Rev.* 131 (1963) 2649.
- [55] S. E. Woosley, W. A. Fowler, J. A. Holmes, and B. A. Zimmerman, unpublished preprint OAP-422, Calif. Inst. Tech. (1975).
- [56] H. Behrens and J. Jänecke, in Landolt-Börnstein Numerical Data and Functional Relationships in Science and Technology, New Series, Group I, Vol. 4, Springer, New York (1969).

Table 1
LEGS Observations Used for Background Calculations

Flight Number	Local Date and Launch Site	Detector Configuration	Aperture ^{a)} Solid Angle (steradians)	Nominal ^{b)} Shield Threshold (keV)	Time Interval Used For Background Measurement (UT)	Instrument ^{c)} Atmospheric Depth (g cm^{-2})	Pointing Angle ^{d)} From Zenith (degrees)
III	1979 May 25 Palestine, Texas	Coaxial	8.0×10^{-2}	100 ^{e)}	5:51-12:10 May 26	4.8-5.1	35-54
V	1980 Sept. 24 Palestine, Texas	Planar	1.5×10^{-2}	100	19:16-2:57 Sept. 24-25	3.0-4.0	3-47

a) From top of detectors. For high-energy photons interacting throughout the coaxial detector volume, the average aperture solid angle is 7.3×10^{-2} sr.

b) The actual shield thresholds in flight may have been as much as a factor of 2 higher.

c) Depth range during background measurement.

d) Pointing angle range during background measurement.

e) 50 keV for bottom "plug" section of shield.

Table 2
Passive Material Inside LEGS Shield

Item	Material	Mass (g)	Detector Configuration
Cryostat	Al	695	Coaxial
	Stainless	930	
Detector Housings	Al	700	Planar
	Al	380	Coaxial
Ge Deadlayer	Al	150	Planar
	Ge	370	Coaxial
Coldfinger	Ge	125	Planar
	Cu	55	Both
Shield Housing	Al	2000-3400 ^{a)}	Both
Passive Collimator	Fe	4800	Planar

a) Range of values represents uncertainty in thickness of housing walls.
Minimum thickness is estimated at 0.16 cm and maximum thickness at 0.32 cm.

Table 3
Sources of Increase in Aperture Flux Background
for Coaxial Detectors

Source	Mass (g)	Background ^{a)} Increase (%)
Single Scattering in Passive Materials		
Ge Deadlayer	370	14.9
Al Detector Housing	380	5.8
Al Cryostat	695	6.1
Steel Baseplate	930	3.8
Al Shield Housing ^{b)}	3400	8.0
Multiple Scattering in Passive Materials		13.2
Scattering in Shield, $\Delta E < 200$ keV ($\Delta E < 100$ keV)		18.8 <u>(6.8)</u>
Total, 200 keV Threshold		70.6

a) In 0.1 to 1.0 MeV energy range.

b) Thick (0.32 cm) shield housing case.

Table 4

Interactions Contributing to β^- Decay Background

Number ^{a)}	Interaction or Product	Event ^{b)} Type	β^- Half-Life	Branching Percentage	Decay ^{c)} Mode	Forbiddenness	Endpoint ^{d)} Energy (MeV)	Rate ^{f)} (Decays $s^{-1}cm^{-3}$)	References
1	$^{76}Ge(n, \gamma)^{77m}Ge$	λ	53s	80	72.5% gs	Allowed	2.86	1.99×10^{-4}	Note 1
2		n			26.3% 0.216	"	2.65	3.10×10^{-5}	
3	$^{77}Ge(\beta^-)^{77}As$	λ	38.8h	100	97.5% gs	"	0.69	3.27×10^{-5}	Note 2
s	$^{76}Ge(n, p)^{76}Ga$	n	27.1s	100	14% 0.563	1 st f.n.u.	6.21	1.93×10^{-8}	32
s		n			3.8% 1.108	"	5.66	3.15×10^{-9}	
s	$^{76}Ge(n, np)^{75}Ga$	n	2.10m	100	44% 0.253	Allowed	3.05	$< 1.7 \times 10^{-7}$ g)	32
4	$^{76}Ge(n, 2n)^{75}Ge$	λ	82.8m	100	87% gs	"	1.18	3.88×10^{-4}	32, 29-31
5		n			10.8% 0.265	"	0.91	1.67×10^{-5}	
s	$^{76}Ge(n, \alpha)^{73}Zn$ h)	?	24s	100	?	?	~4.7	$\sim 1.3 \times 10^{-6}$	32
s	$^{73}Zn(\beta^-)^{73}Ga$	λ	4.9h	100	44% ms	Allowed	1.49	$\sim 3.2 \times 10^{-7}$	Note 2
s		n			47% 0.297	"	1.20	$\sim 1.1 \times 10^{-7}$	
6	$^{74}Ge(n, \gamma)^{75}Ge$	λ	82.8m	100	87% gs	"	1.18	3.89×10^{-3}	Note 3
7		n			10.8% 0.265	"	0.91	1.67×10^{-4}	
s	$^{74}Ge(n, p)^{74}Ga$	n	8.1m	100	5% 0.596	1 st f.u.	4.80	1.43×10^{-7}	32, 31
s	$^{74}Ge(n, np)^{73}Ga$	λ	4.9h	100	44% ms	Allowed	1.49	$< 5.3 \times 10^{-6}$ g)	32
s		n			47% 0.297	"	1.20	$< 1.7 \times 10^{-6}$	
8	$^{74}Ge(n, \alpha)^{71}Zn$	λ	2.4m	100	57% gs	"	2.82	3.28×10^{-5}	32, 29, 31
9		n			27.3% 0.512	"	2.31	2.48×10^{-6}	
10	$^{73}Ge(n, p)^{73}Ga$	λ	4.9h	100	44% ms	"	1.49	2.43×10^{-6}	32, 31
s		n			47% 0.297	"	1.20	8.04×10^{-7}	
s	$^{73}Ge(n, np)^{72}Ga$	n	14.1h	100	11% 0.834	1 st f.n.u.	3.16	$< 2.3 \times 10^{-8}$ g)	32

Number	Interaction or Product	Event Type	β^- Half-Life	β^- Branching Percentage	Decay Mode	Forbiddenness	Endpoint Energy (MeV)	Rate (Decays $s^{-1}cm^{-3}$)	References	
										Decay
S	$^{72}Ge(n,p)^{72}Ga$	n	14.1h	100	11%	0.834	1 st f.n.u.	3.16	1.69x10 ⁻⁷	32,29,31
11	$^{72}Ge(n,\alpha)^{69}Zn$	α	56m	100	100%	gs	Allowed	0.90	1.63x10 ⁻⁵	32,29,31
12	$^{70}Ge(n,p)^{70}Ga$	α	21.1m	99.8	99.3%	gs	"	1.66	1.32x10 ⁻⁴	32,29,31
S	$^{76}Ge(p,n)^{76}As$	α	26.3h	100	51%	gs	1 st f.u.	2.97	1.79x10 ⁻⁶	33,34
S		n			36%	0.559	1 st f.n.u.	2.41	1.77x10 ⁻⁷	
13	$^{76}Ge(p,2p)^{75}Ga$	n	2.10m	100	44%	0.253	Allowed	3.05	5.26x10 ⁻⁶	33,34
14	$^{75}Ga(\beta^-)^{75}Ge$	α	82.8m	100	87%	gs	"	1.18	2.75x10 ⁻⁵	Note 2
S		n			10.8%	0.265	"	0.91	1.23x10 ⁻⁶	
15	$^{76}Ge(p,np)^{75}Ge$	α	82.8m	100	87%	gs	"	1.18	1.65x10 ⁻⁴	33,34
16		n			10.8%	0.265	"	0.91	7.10x10 ⁻⁶	
17	$^{76}Ge(p,\alpha)^{73}Ga$	α	4.9h	100	44%	ms	"	1.49	1.97x10 ⁻⁵	33,34
18		n			47%	0.297	"	1.20	6.12x10 ⁻⁶	
S	$^{74}Ge(p,n)^{74}As$	α	17.8d	32	53%	gs	1 st f.u.	1.35	1.82x10 ⁻⁷	33,34
S		n			47%	0.635	1 st f.n.u.	0.72	1.94x10 ⁻⁸	
19	$^{74}Ge(p,2p)^{73}Ga$	α	4.9h	100	44%	ms	Allowed	1.49	4.74x10 ⁻⁵	33,34
20		n			47%	0.297	"	1.20	1.47x10 ⁻⁵	
S	$^{73}Ge(p,2p)^{72}Ga$	n	14.1h	100	11%	0.834	1 st f.n.u.	3.16	9.86x10 ⁻⁸	33,34
21	$^{73}Ge(p,\alpha)^{70}Ga$	α	21.1m	99.8	99.3%	gs	Allowed	1.66	7.77x10 ⁻⁵	33,34
S	^{74}Ga	n	8.1m	100	5%	0.596	1 st f.u.	4.80	1.25x10 ⁻⁶	33,34
22	^{73}Ga	α	4.9h	100	44%	ms	Allowed	1.49	3.82x10 ⁻⁵	33,34
23		n			47%	0.297	"	1.20	1.19x10 ⁻⁵	
24	^{72}Ga	n	14.1h	100	11%	0.834	1 st f.n.u.	3.16	3.39x10 ⁻⁶	33,34
25	^{71}Zn	α	2.4m	100	57%	gs	Allowed	2.82	5.56x10 ⁻⁵	33,34

Number	Interaction or Product	Event Type	β^- Half-Life	β^- Branching Percentage	Decay Mode	Decay Forbiddenness	Endpoint Energy (MeV)	Rate (Decays s ⁻¹ cm ⁻³)	References
26		β^-			27.3% 0.512	Allowed	2.31	4.21x10 ⁻⁶	
27	⁷⁰ Cu	β^-	5s	100	46% gs	"	6.17	5.01x10 ⁻⁵	33,34
28	⁷⁰ Ga	β^-	21.1m	99.8	99.3% gs	"	5.29	4.70x10 ⁻⁷	33,34
29	⁶⁹ Cu	β^-	3.0m	100	79% gs	"	2.48	2.24x10 ⁻⁵	33,34
30	⁶⁹ Cu(β^-) ⁶⁹ Zn	β^-	56m	100	100% gs	"	0.90	2.79x10 ⁻⁵	Note 2
31	⁶⁹ Zn	β^-	56m	100	100% gs	"	0.90	4.66x10 ⁻⁴	33,34
32	⁶⁸ Cu	β^-	31s	100	31% gs	"	4.62	1.93x10 ⁻⁵	33,34
33	⁶⁷ Cu	β^-	61.9h	100	40% 1.077 49.7% local i)	"	3.54	1.49x10 ⁻⁶	33,34
34		β^-			49.3% 0.185	"	0.39	2.30x10 ⁻⁶	
35	⁶⁷ Ni h)	?	18s	100	?	?	-3.8	-1.6 x10 ⁻⁵ ?	33,34
36	⁶⁷ Ni(β^-) ⁶⁷ Cu	β^-	61.9h	100	49.7% local i)	Allowed	-0.5	9.64x10 ⁻⁸	Note 2
37	⁶⁶ Cu	β^-	5.1m	100	49.3% 0.185	"	0.39	4.68x10 ⁻⁸	33,34
38	⁶⁵ Ni	β^-	2.52h	100	92% gs 8% 1.039	"	2.64	2.44x10 ⁻⁴	33,34
39		β^-			61% gs	"	1.60	1.42x10 ⁻⁶	
40		β^-			23% 1.482	"	0.66	5.46x10 ⁻⁵	33,34
41		β^-			9.8% 1.115	"	1.02	1.24x10 ⁻⁶	
42	⁶⁴ Cu	β^-	12.7h	40	100% gs	"	0.58	8.42x10 ⁻⁵	33,34
43	⁶² Co	β^-	1.5m	100	64% 1.173	"	4.14	7.04x10 ⁻⁷	33,34
44	⁶¹ Co	β^-	1.65h	100	96.4% local j)	"	1.25	5.84x10 ⁻⁵	33,34

Number	Interaction or Product	Event Type	β^- Half-Life	β^- Branching Percentage	Decay Mode	Decay Forbiddenness	Endpoint Energy (MeV)	Rate (Decays $s^{-1}cm^{-3}$)	References
39	^{57}Mn	λ	1.6m	100	80.8% 10ca1k)	Allowed	2.68	1.47×10^{-5}	33,34
40		n			11.5% -0.13	"	-2.56	1.44×10^{-6}	
41	^{56}Mn	n	2.58h	100	56%	"	2.85	2.55×10^{-6}	33,34
42	^{55}Cr	λ	3.55m	100	100% gs	"	2.60	1.01×10^{-5}	33,34
S	^{52}V	n	3.75m	100	99.2%	"	2.54	1.07×10^{-7}	33,34
43	^{42}K	λ	12.36h	100	81% gs	1stf.u.	3.52	9.68×10^{-6}	33,34
S		n			18%	1stf.n.u.	2.00	9.46×10^{-8}	
44	^{38}Cl	λ	37.3m	100	58% gs	1stf.u.	4.92	1.10×10^{-5}	33,34
S		n			11%	1stf.n.u.	2.75	6.26×10^{-8}	
45	^{34}p	λ	12.4s	100	85% gs	Allowed	5.38	7.88×10^{-5}	33,34
S		n			15%	"	3.25	4.17×10^{-8}	
46	^{31}Si	λ	2.62h	100	99.9% gs	"	1.49	2.29×10^{-5}	33,34
S	^{29}Al	n	6.6m	100	89%	"	2.41	9.68×10^{-7}	33,34
47	^{28}Al	n	2.24m	100	100%	"	2.86	2.55×10^{-5}	33,34
S	^{27}Mg	n	9.46m	100	72%	"	1.77	1.46×10^{-6}	33,34
S		n			27%	"	1.59	3.28×10^{-7}	
48	^{25}Na	λ	60s	100	63% gs	"	3.83	1.08×10^{-5}	33,34
S		n			24%	"	-2.5	2.14×10^{-7}	
49	^{23}Ne	λ	37.6s	100	67% gs	"	4.37	1.14×10^{-5}	33,34
S		n			32%	"	3.93	1.09×10^{-5}	
50	^{21}F	λ	4.32s	100	29% gs	"	5.69	4.34×10^{-6}	33,34
51		n			63%	"	5.34	2.45×10^{-6}	
52	^{20}F	n	11.0s	100	100%	"	5.39	2.02×10^{-6}	33,34

Number	Interaction or Product	Event Type	β^-		Decay Mode	Decay Forbiddenness	Endpoint Energy (MeV)	Rate (Decays $s^{-1}cm^{-3}$)	References	
			Half-Life	Branching Percentage						
53	^{19}O	n	26.9s	100	40%	0.197	Allowed	4.62	2.39×10^{-6}	33,34
54	^{17}N	λ	4.17s	100	95%	n	"	~3.7	1.12×10^{-5}	33,34
55	^{16}N	λ	7.13s	100	26%	gs	1 st f.u.	10.42	1.09×10^{-5}	33,34
S	^{15}C	n	2.45s	100	68%	6.129	Allowed	4.29	8.56×10^{-7}	33,34
56	^{13}B	λ	17.4ms	100	32%	gs	1 st f.n.u.	9.77	3.45×10^{-6}	33,34
S	^{13}B	n	17.4ms	100	68%	5.299	Allowed	4.47	2.20×10^{-7}	33,34
57	^{13}B	λ	17.4ms	100	92%	gs	"	13.44	1.17×10^{-5}	33,34
S	^{12}B	n	20.4ms	100	8%	3.68	"	9.76	4.07×10^{-8}	33,34
58	^{12}B	λ	20.4ms	100	97.1%	gs	"	13.37	4.89×10^{-5}	33,34
59	^{11}Be	λ	13.8s	100	57%	gs	1 st f.n.u.	11.51	6.36×10^{-6}	33,34
S	^{11}Be	n	13.8s	100	29%	2.125	"	9.38	1.62×10^{-7}	33,34
60	9Li	λ	0.18s	100	100%	local λ)	Allowed	~13.	1.52×10^{-5}	33,34
61	8Li	λ	0.84s	100	100%	local λ)	"	13.07	4.52×10^{-5}	33,34
62	6He	λ	0.81s	100	100%	gs	"	3.51	1.27×10^{-4}	33,34

a) Listed numbers correspond to those in Figure 18. An "s" is given for small components with rates less than $\sim 1.5 \times 10^{-6} s^{-1} cm^{-3}$.

b) λ = localized decays, n = nonlocalized decays

c) gs = ground state, ms = metastable state, n = neutron. Numbers given are energies (in MeV) of prompt photons accompanying the decay. Decays with more than one prompt photon have low rates, and are not listed. (Example: 58% gs, 21% 0.216 - 58% of decays are to ground state, 21% are accompanied by a prompt 0.216 MeV photon, and the rest are accompanied by more than one prompt photon.)

- d) f. = forbidden, u. = unique, n.u. = nonunique (see, e.g., Behrens and Szybisz [36]).
- e) Endpoint energy of beta decay; mass difference minus excitation energy of daughter nuclide.
- f) Rate of β^- -decay events in LEGS detectors 6 hours after balloon ascends through Pfotzer maximum. Events with simultaneous interactions in the shield are vetoed and not included. With few exceptions, only interactions with rates greater than $5 \times 10^{-8} \text{ s}^{-1} \text{ cm}^{-3}$ are listed.
- g) Upper limits only can be calculated due to uncertainties in interaction cross sections. In all cases rate upper limit is low enough to neglect interaction.
- h) Unknown decay mode. Rate is small enough in both cases to neglect.
- i) ^{67}Cu - "local" decays are 20% gs, $\sim 7.7\%$.093 MeV internal conversion electron, $\sim 15.3\%$.093 MeV photon, and 6.7% .091 MeV photon/electron plus 0.093 MeV photon/electron. Photons are absorbed within ~ 3 mm and electrons within $\ll 1$ mm, which are considered local in this study.
- j) ^{61}Co - decays accompanied by .067 MeV photon which is absorbed within ~ 2 mm.
- k) ^{57}Mn - decays accompanied by .014 MeV photon which is absorbed within $\ll 1$ mm.
- l) ^9Li and ^8Li - decays accompanied by neutrons which generally escape undetected, and alphas particles which have ranges $\ll 1$ mm.

Note 1 - The ^{77m}Ge β^- decay rate was derived from the measured strength of the 0.160 MeV line in the spectrum produced via $^{76}\text{Ge}(n,\gamma)^{77m}\text{Ge}(\gamma)^{77}\text{Ge}$. The ratio of β^- to γ decays of ^{77m}Ge is 4, the total-absorption efficiency for 0.160 MeV photons produced in the LEGS detector is 0.62, the detector volume is 230 cm^3 , the 0.160 MeV line strength for flight III was $9.8 \times 10^{-3}\text{ s}^{-1}$, and 0.725 of the β^- decays are to the gs, giving $1.99 \times 10^{-4}\text{ s}^{-1}\text{ cm}^{-3}$ decays to the gs. Decays from ^{77}Ge are not listed because their rate is very small due to the long half-life (11.3h) and the many prompt gamma rays accompanying each decay.

Note 2 - The decay rates of β^- -unstable nuclides produced via a previous β^- decay were calculated using the production rate of the intermediate nuclide.

Note 3 - The ^{75}Ge β^- decay rate was derived from the measured strength of the 0.140 MeV line in the spectrum produced via $^{74}\text{Ge}(n,\gamma)^{75m}\text{Ge}(\gamma)^{75}\text{Ge}$ and via $^{76}\text{Ge}(n,2n)^{75m}\text{Ge}(\gamma)^{75}\text{Ge}$. The line strength in flight III was 0.378 s^{-1} , of which 0.087 s^{-1} was from the $(n,2n)$ interaction (calculated using IAEA cross sections [30]), giving an (n,γ) rate of 0.291 s^{-1} . The (n,γ) cross section for producing ^{75}Ge is 2.25 times that for ^{75m}Ge (Table of Isotopes) so that the total ^{75}Ge production rate is 3.25 times that for ^{75m}Ge (the ^{75m}Ge half-life is short compared with that of ^{75}Ge). The total-absorption efficiency for the 0.140 MeV line is 0.87 (58% of the line is internal conversion electrons), the ^{75}Ge half-life is 82.8m giving a decay rate after 6 hours of .95 times the equilibrium rate, and 0.87 of the decays are to the gs, giving, finally, $3.89 \times 10^{-3}\text{ s}^{-1}\text{ cm}^{-3}$ decays to the gs (detector volume = 230 cm^3).

Figure Captions

Figure 1 - Observed and calculated background in the LEGS coaxial array. The count rate spectrum was divided by the volume of active Ge in the detectors (230 cm^3) to give units of $\text{cnts s}^{-1} \text{ MeV}^{-1} \text{ cm}^{-3}$. The data are from flight III (Palestine, Texas; 5 g cm^{-2}), and the calculations are for the continuum background underlying the background lines. The elastic neutron scattering, aperture flux, β^- decays localized and nonlocalized, and shield leakage components of the calculation are shown separately.

Figure 2 - Same as Figure 1, but for the LEGS planar array flight V (Palestine, Texas; 3.5 g cm^{-2}). The Ge active volume for the planar array is 57 cm^3 .

Figure 3 - Measurements of the total downward gamma-ray flux at 5 g cm^{-2} over Palestine, Texas. The solid line fits the data of Kinzer [14], Kinzer et al. [15], and Schönfelder et al. [16], and is the spectrum used in this paper. The three points from Lockwood et al. [17] have been multiplied by a factor of 1.15 [18] to correct for a depth of 3.5 g cm^{-2} . The points from Ryan et al. [19] and White et al. [20] were measured at a zenith angle of 15° , but no correction was required since the zenith angle flux distribution is approximately flat between 0° and 70° [18,21].

Figure 4 - Neutron and proton spectra inside the LEGS shield during flights III and V. The residual atmosphere above the instrument plus the shield are equivalent to $\sim 35 \text{ g cm}^{-2}$ of air. The ordinate is the omnidirectional flux, which is the total flux incident on a unit sphere. The solid lines show the spectra used in this paper.

Figure 5 - The elastic neutron scattering cross section as a function of incident neutron energy for scatterings which give a Ge atom recoil energy of .04 MeV and .17 MeV. Also shown for aid in defining the shape of the curve at $E_n > 10$ MeV, are cross sections for Cu. The solid lines are the power-law approximations of the data used in this paper. The data are from Garber et al. [38].

Figure 6 - The fraction of the recoil energy lost to signal-producing ionizing collisions for elastic neutron scattering in Ge. The curve was calculated with equation (4).

Figure 7 - The ratio of total aperture flux background to that produced by unscattered photons for the LEGS coaxial and planar detector arrays.

"Unscattered photons" means those that interact only in the detector, and not in the passive material or in the shield. The results were calculated using the Monte Carlo code to simulate the interaction of incident photons with the instrument. The error bars represent statistical uncertainties in the Monte Carlo results. For the coaxial array, the range in possible values due to uncertainties in the shield housing thickness and shield threshold are shown by the two curves. For the planar array, this range is smaller than the statistical uncertainties in the simulation and is therefore not shown.

Figure 8 - Total shield leakage backgrounds, including scatterings in passive material near the detectors and in the shield ($\Delta E < \text{shield threshold}$), compared with the unscattered component for the LEGS coaxial array.

Figure 9 - The effect on the shield leakage background of raising the threshold level in the shield. The ratio of the shield leakage background for a given shield threshold to the background for a 0 keV threshold is shown as a function of the threshold for three different energy ranges. The error bars represent typical absolute uncertainties in the points; the relative uncertainties between points on a given curve are smaller.

Figure 10 - The calculated continuum background and its components in three different modes for the future instrument configuration described in the text. The background is given per unit volume of Ge, with relevant detector volumes for each mode shown. The plotted backgrounds are for events that have no shield coincidences and that satisfy the segment conditions for each mode. The segment conditions are a) all events accepted - no conditions on segments, b) only events with energy deposition in top segment and none in bottom six segments, and c) only events with energy deposition in more than one segment.

Figure 11 - Typical gamma-ray and background events in a multisegment detector. By requiring signal in more than one segment, the background from localized β^- decays is eliminated while the signal from incident gamma rays is kept.

Figure 12 - Full-energy-peak efficiencies for a 7 cm detector with 7 1-cm segments for the three segment coincidence modes.

Figure 13 - The narrow-line ($\Delta E=4$ keV) sensitivity for three segment modes for the instrument described in the text, flown at 3.5 g cm^{-2} over Palestine,

Texas. The upper panel gives the sensitivity improvement for the top-segment and multiple-segment modes compared with the all-events (unsegmented detector) mode. The curves do not apply at energies of strong background lines.

Figure 14 - The sensitivity improvement factor obtained with segmented detectors relative to unsegmented detectors as a function of the number of segments (or segment thickness) at three energies. Panel (a) is for the top-segment mode, and panels (b) and (c) for the multiple-segment mode. The instrument configuration is the same as that assumed for Figures 10 and 13, with the filled circle on each curve corresponding identically to the ratio at that energy in Figure 13. In all cases, except the +'s in panels (b) and (c) equal-size segments were assumed. The +'s correspond to a 2-segment detector with 1 cm top-segment thickness and 6 cm bottom-segment thickness. The open circles in panels (b) and (c) are the improvement factors if the multiple-segment events in a 7-segment detector are divided into those that include the top-segment and those that do not. Similar points above the curve occur for other multisegment detectors, but are not plotted.

Figure 15 - The sensitivity improvement factor obtained with segmented detectors relative to unsegmented detectors as a function of detector diameter at two energies. The detectors were assumed to be cylinders with diameter equal to height, and divided into 1 cm segments. The shield configuration is the same as that assumed for Figures 10 and 13. The filled circles on the curves correspond identically to the ratios at those energies in Figure 13. The absolute sensitivities ($\text{ph cm}^{-2} \text{s}^{-1}$) for an unsegmented detector ranges from (a) 1.1×10^{-4} for 5 cm diameter to 7.8×10^{-5} for 8 cm at 0.2 MeV, and (b) 2.1×10^{-4} for 5 cm to 9.4×10^{-5} for 8 cm at 1 MeV.

Figure 16 - The sensitivity improvement factor obtained with segmented detectors relative to unsegmented detectors as a function of shield thickness and threshold for two energies. Apart from the shield, the instrument configuration is the same as that assumed in Figures 10 and 13, with the filled circles corresponding identically to the ratios at those energies in Figure 13. The absolute sensitivities ($\text{ph cm}^{-2} \text{s}^{-1}$) for the unsegmented detectors range from (a) 9.9×10^{-5} for 10 cm thickness to 8.7×10^{-5} for 20 cm at 0.2 MeV, (b) 1.7×10^{-4} for 10 cm to 1.1×10^{-4} for 20 cm at 1 MeV, (c) 8.6×10^{-5} for 0 keV threshold to 9.1×10^{-5} for 180 keV at 0.2 MeV, and (d) 1.2×10^{-4} for 0 keV to 1.3×10^{-4} for 180 keV at 1 MeV.

Figure 17 - The probability that gamma rays produced internal to a detector are fully absorbed in the detector, for two different detector sizes. The LEGS coaxial detector is approximately 4.6 cm diameter by 4.6 cm length, and the 7 cm coaxial detector is 7 cm diameter by 7 cm length.

Figure 18 - Components of the β^- -decay background. Identification and relevant data for each decay spectrum are given in Table 4. The short-dashed curves are localized decays and the long-dashed curves are nonlocalized. The sum of the localized decays is shown by the solid curve in panel (a).

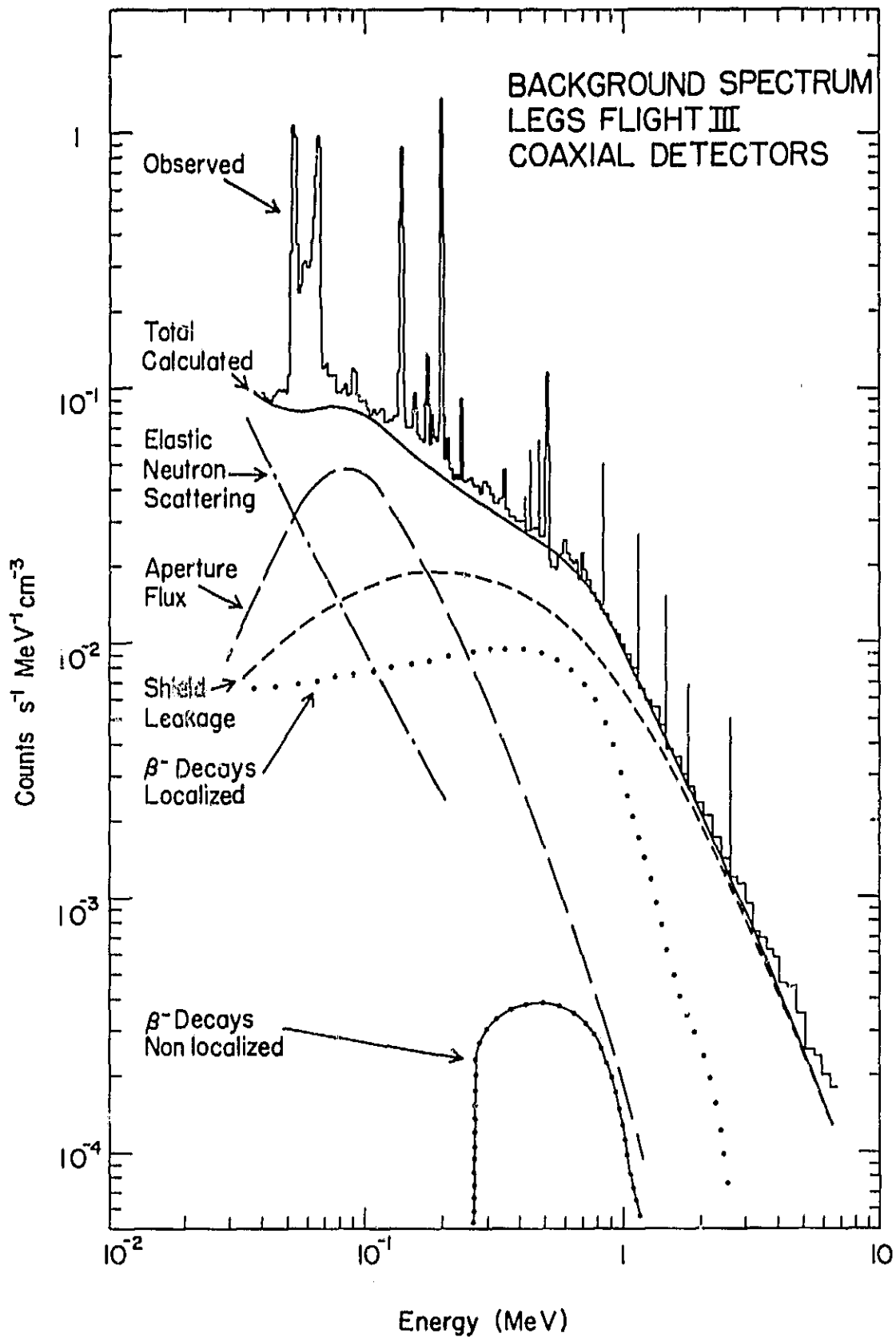


Figure 1

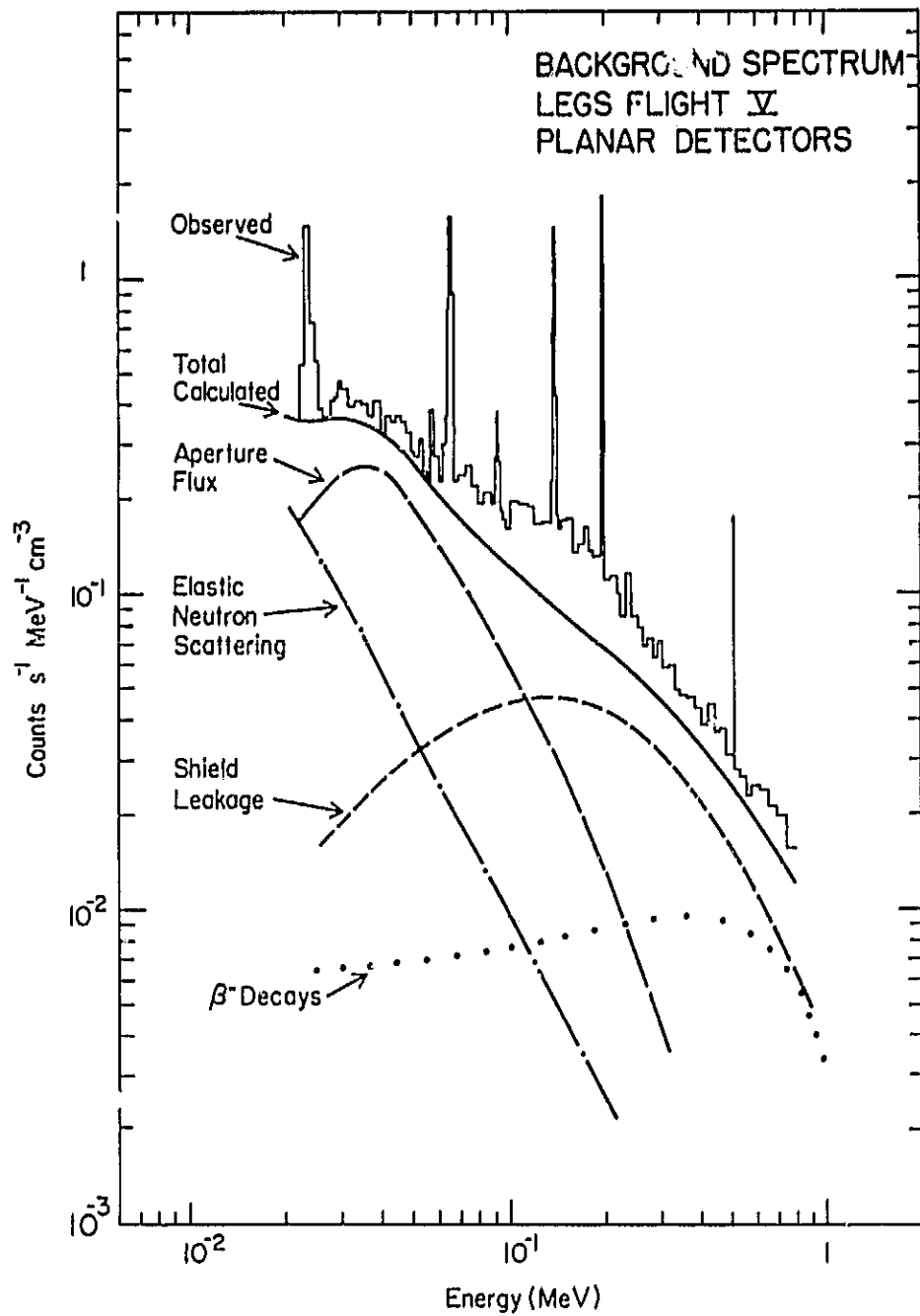


Figure 2

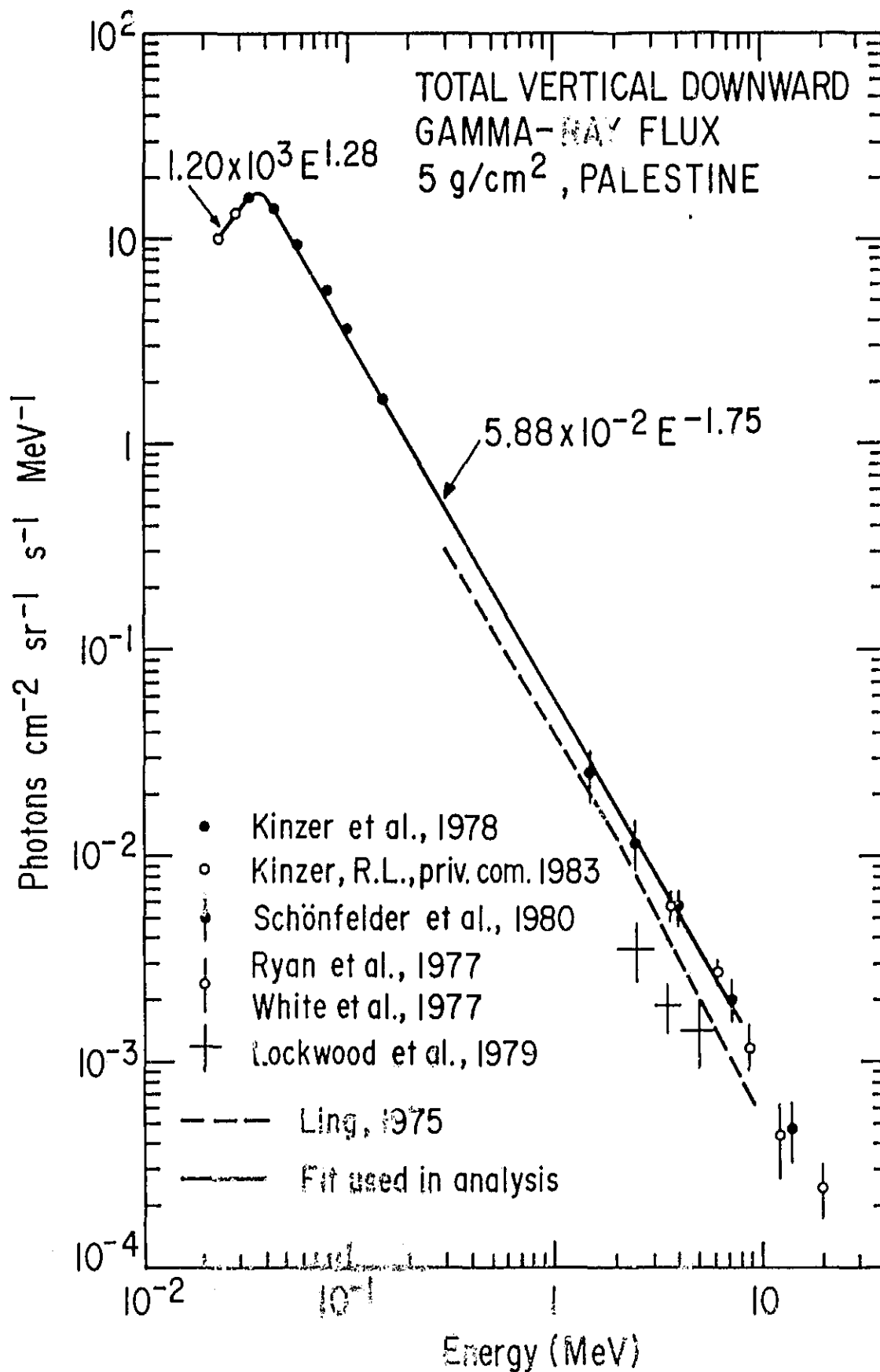


Figure 3

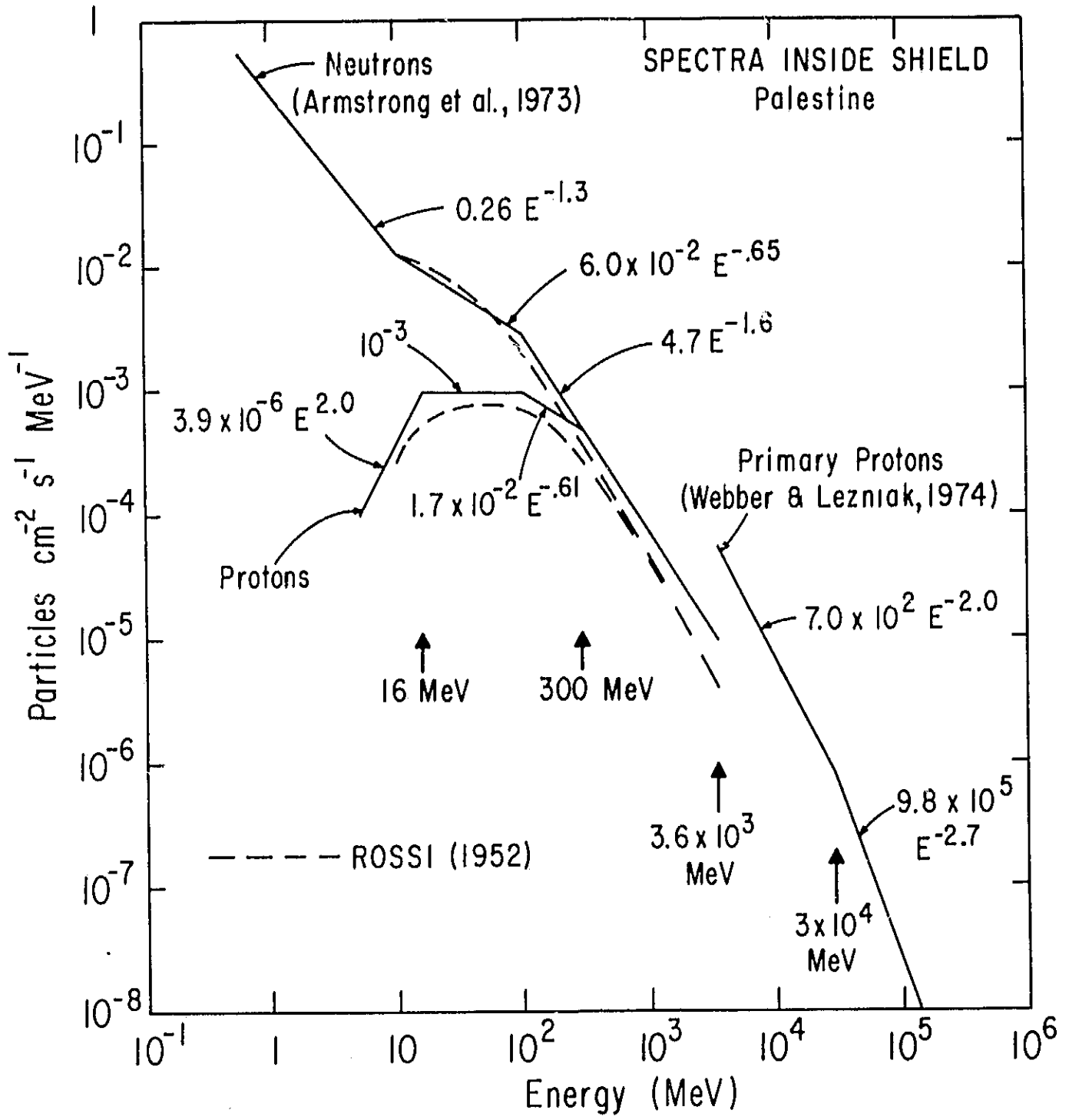


Figure 4

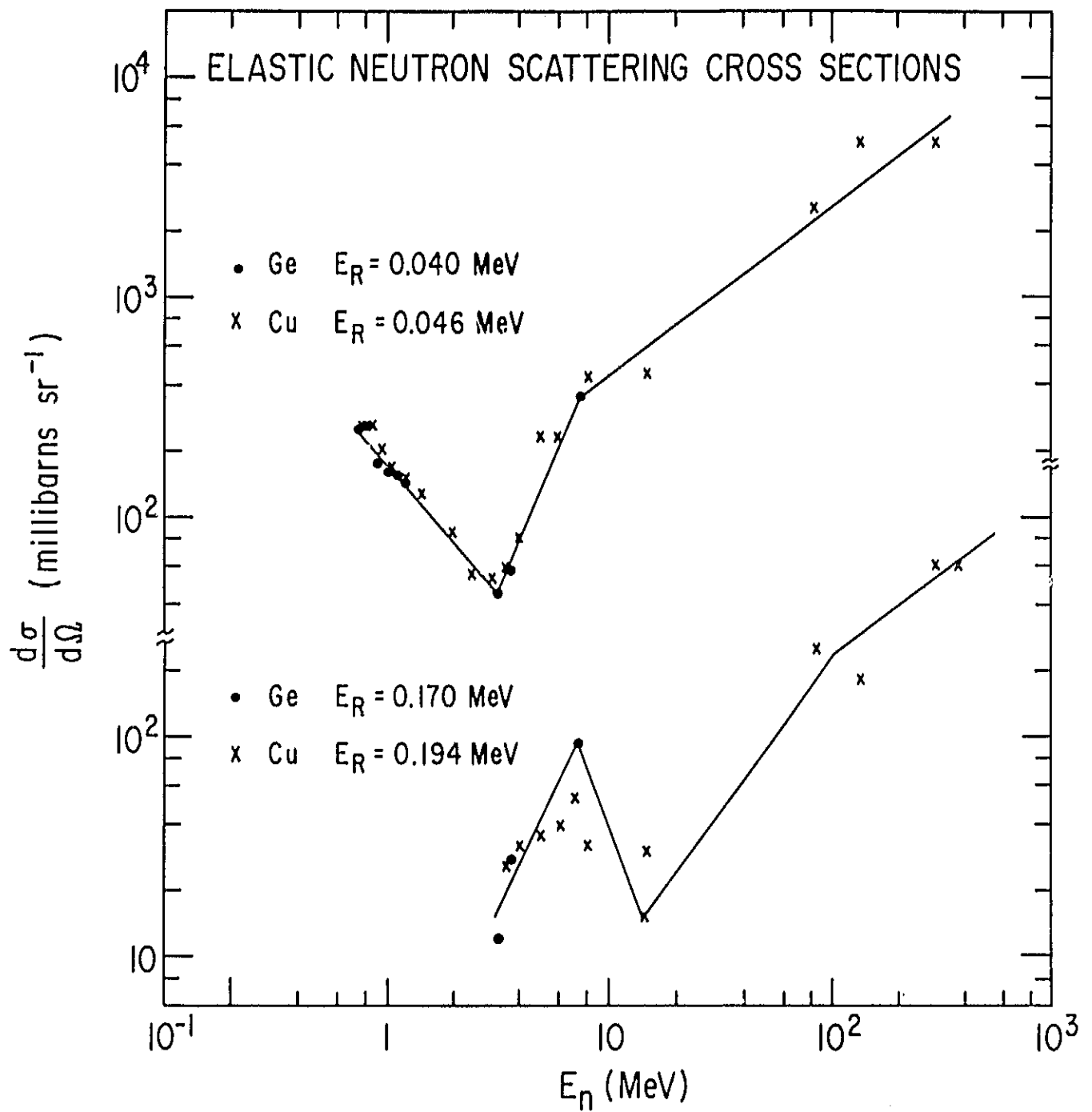


Figure 5

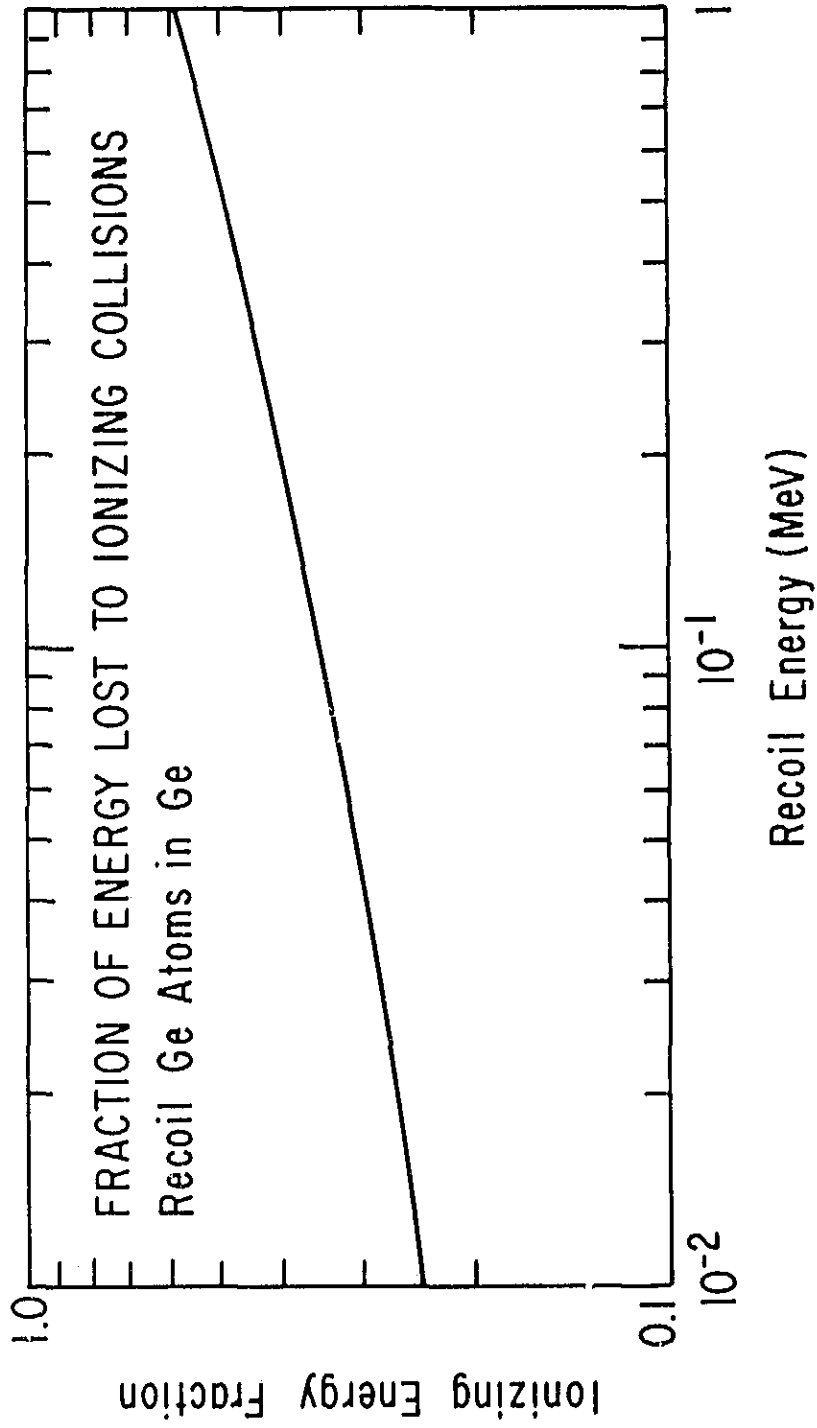


Figure 6

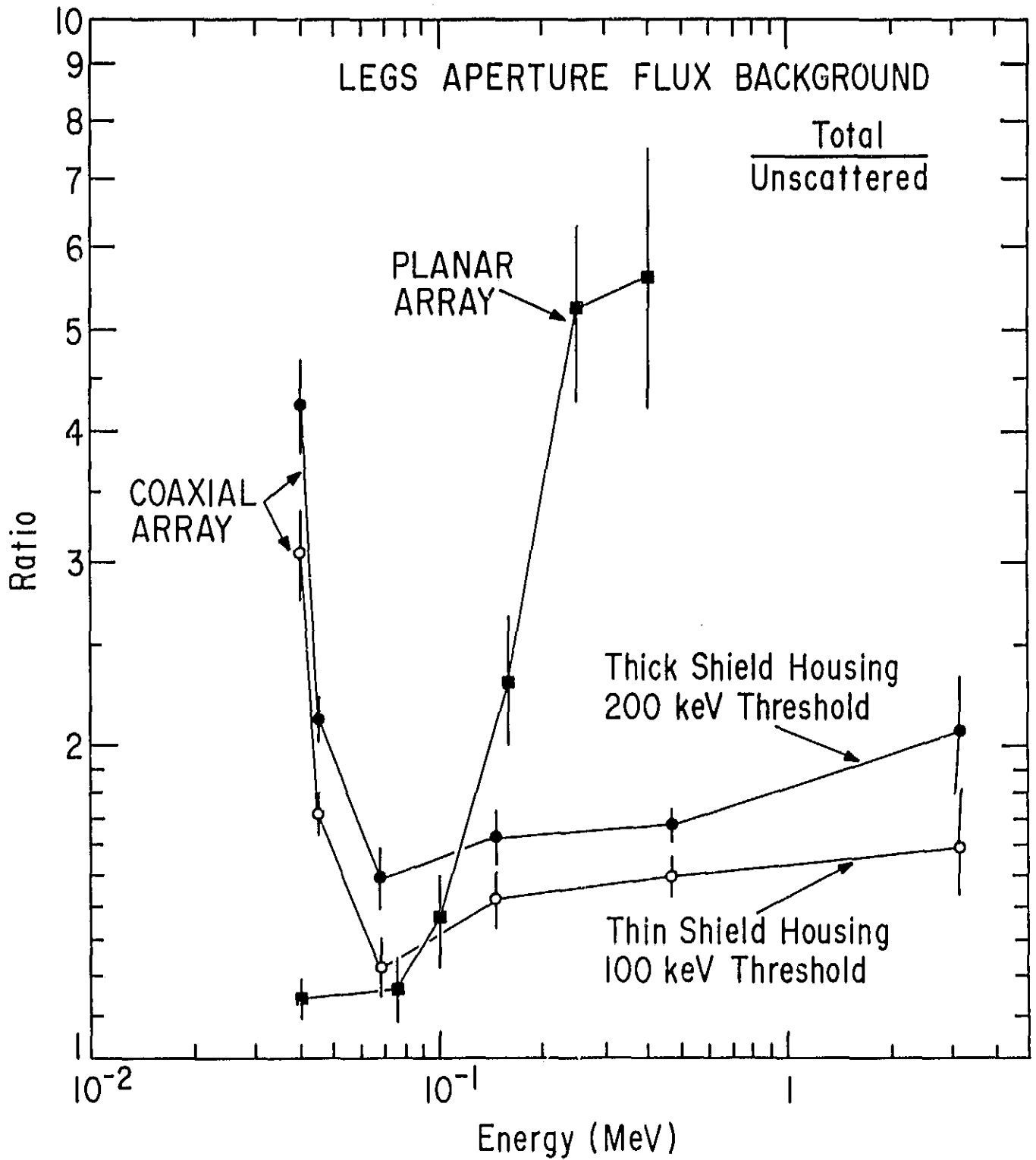


Figure 7

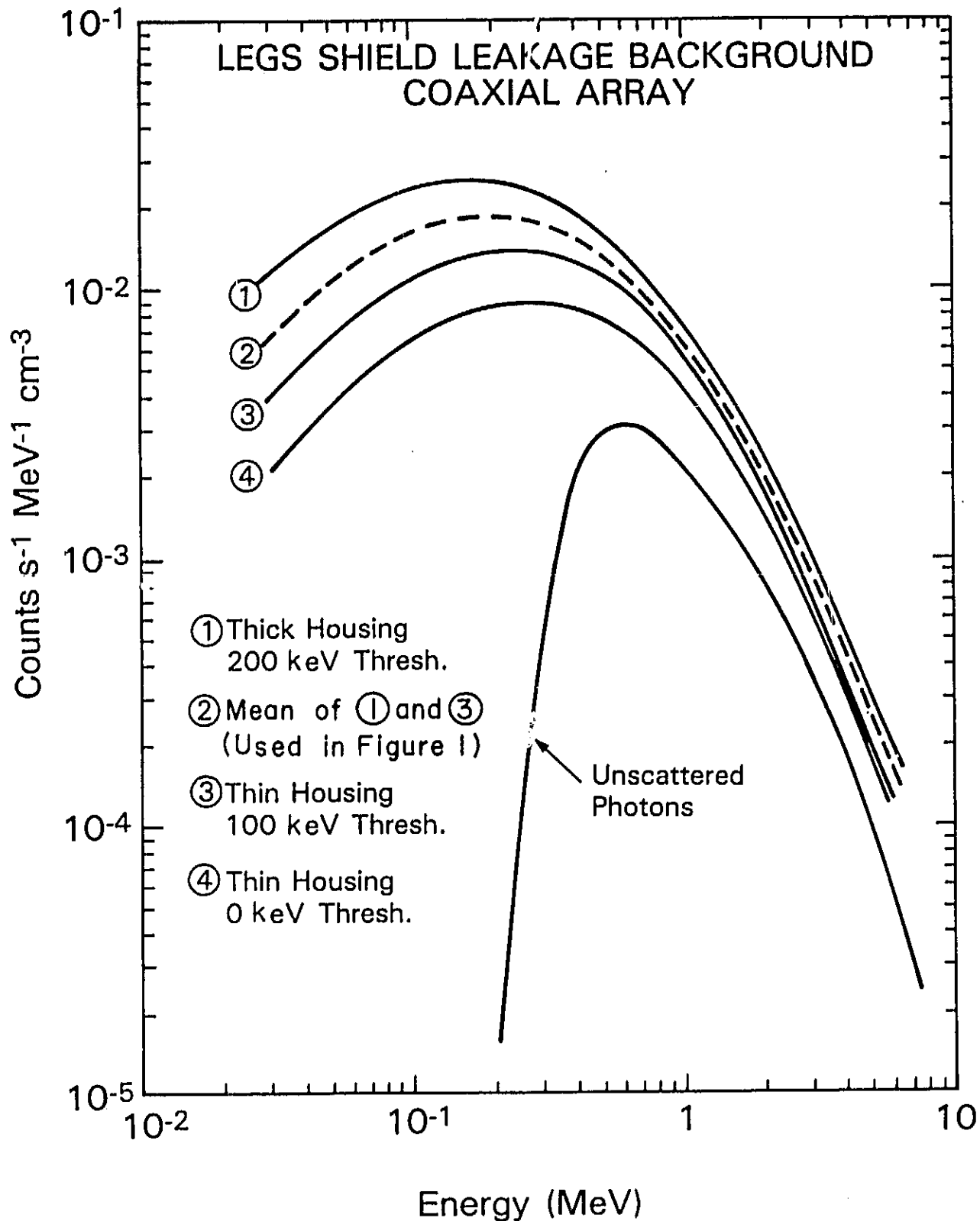


Figure 8

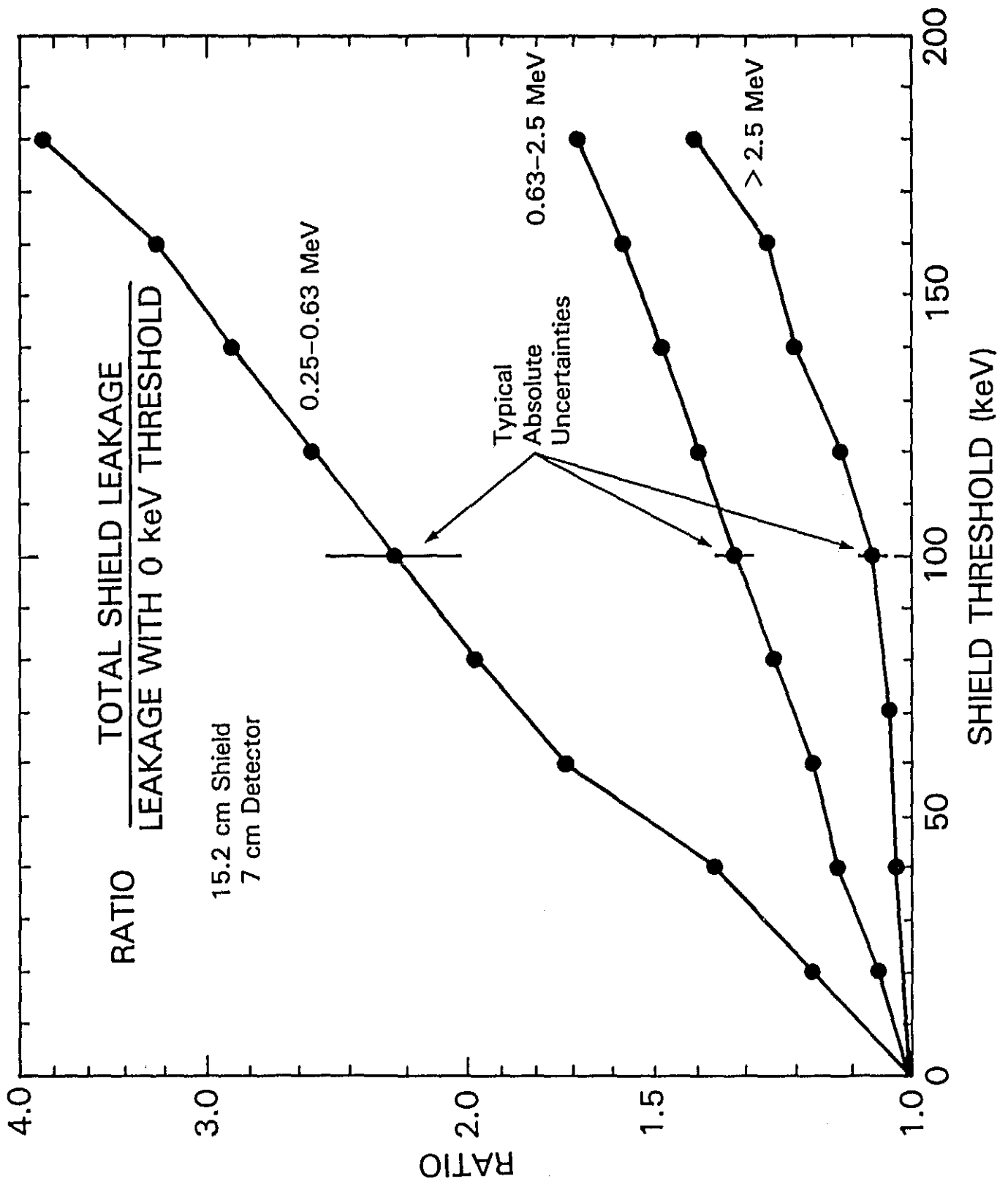


Figure 9

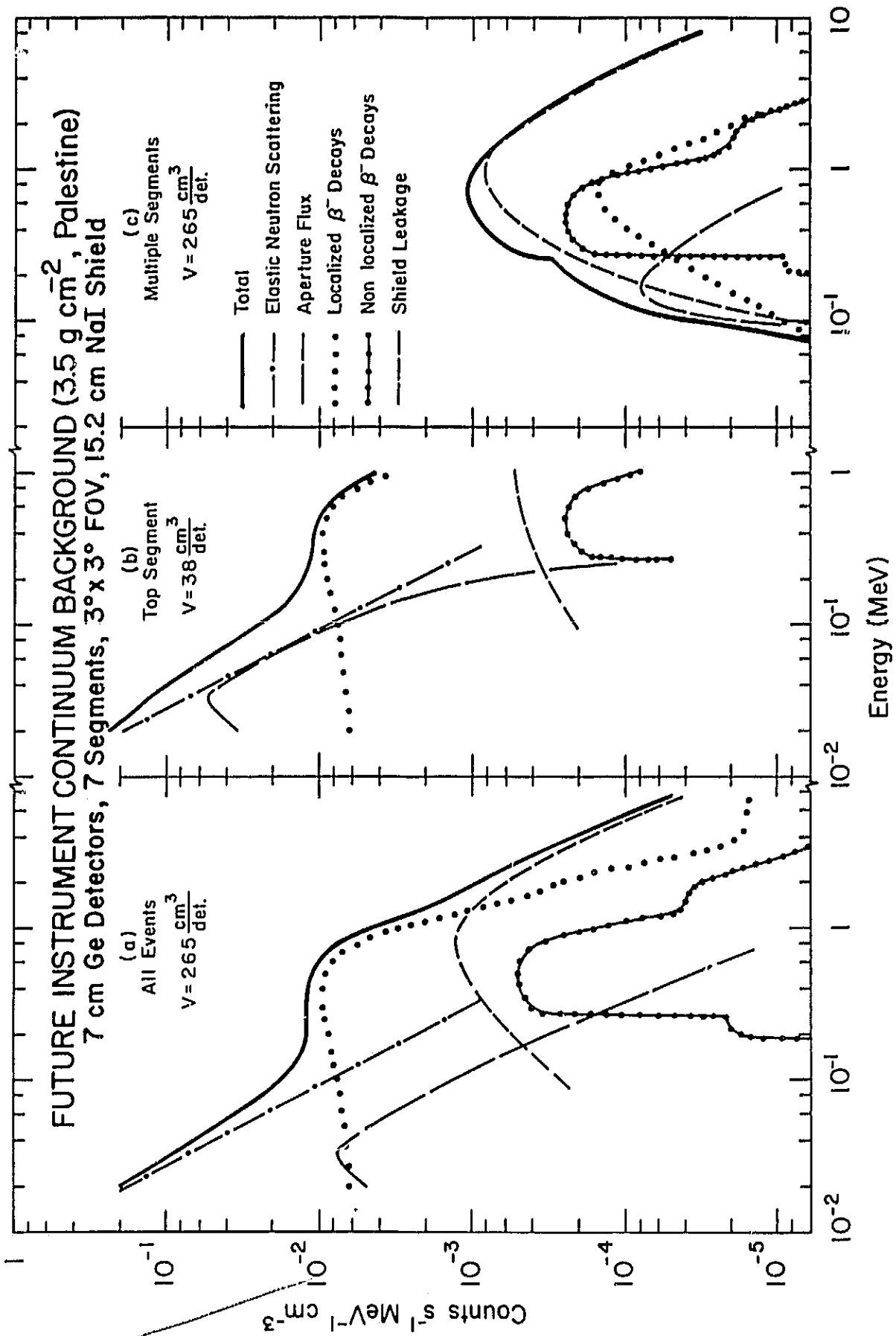


Figure 10

MULTIPLE-SEGMENT MODE

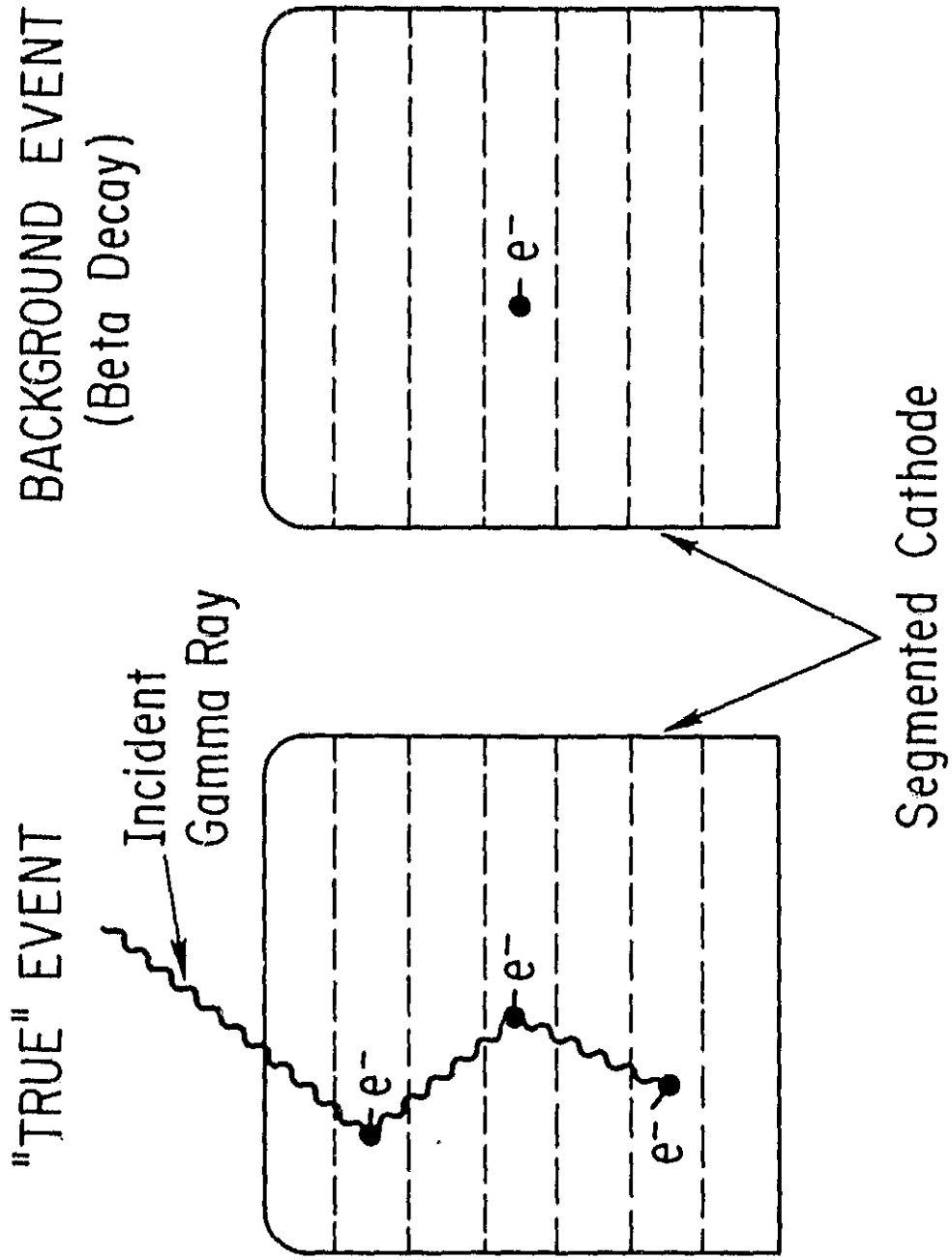


Figure 11

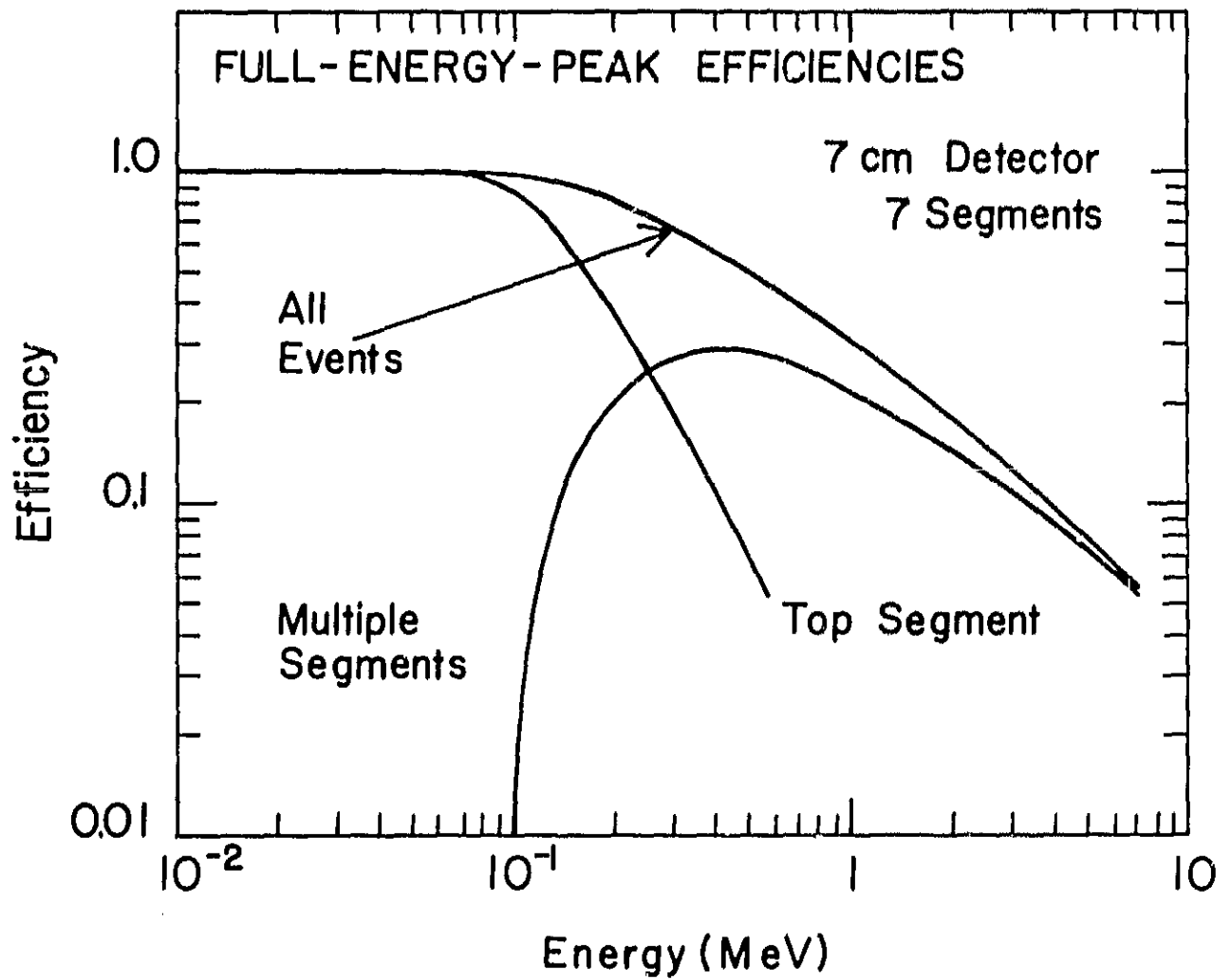


Figure 12

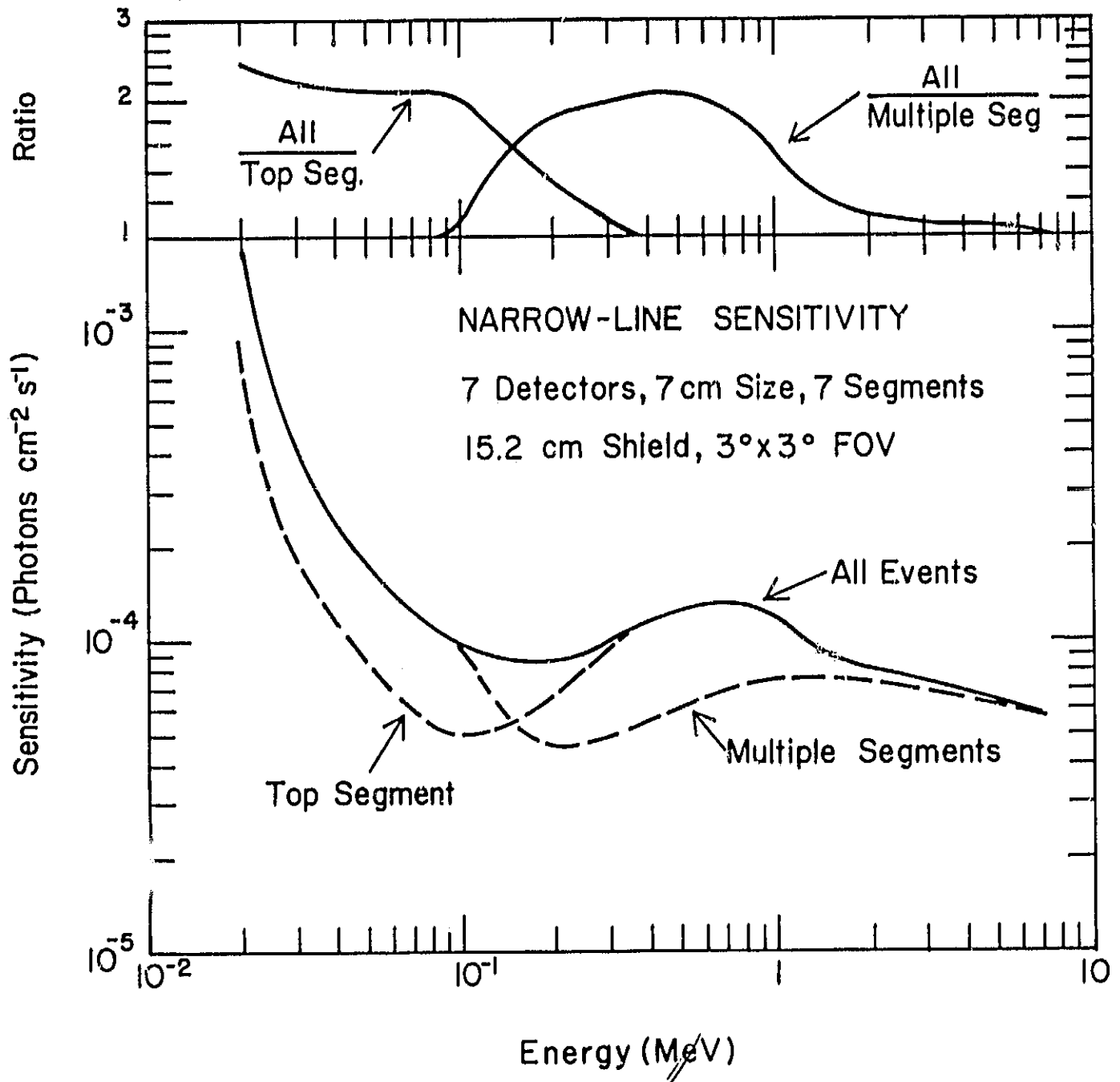


Figure 13

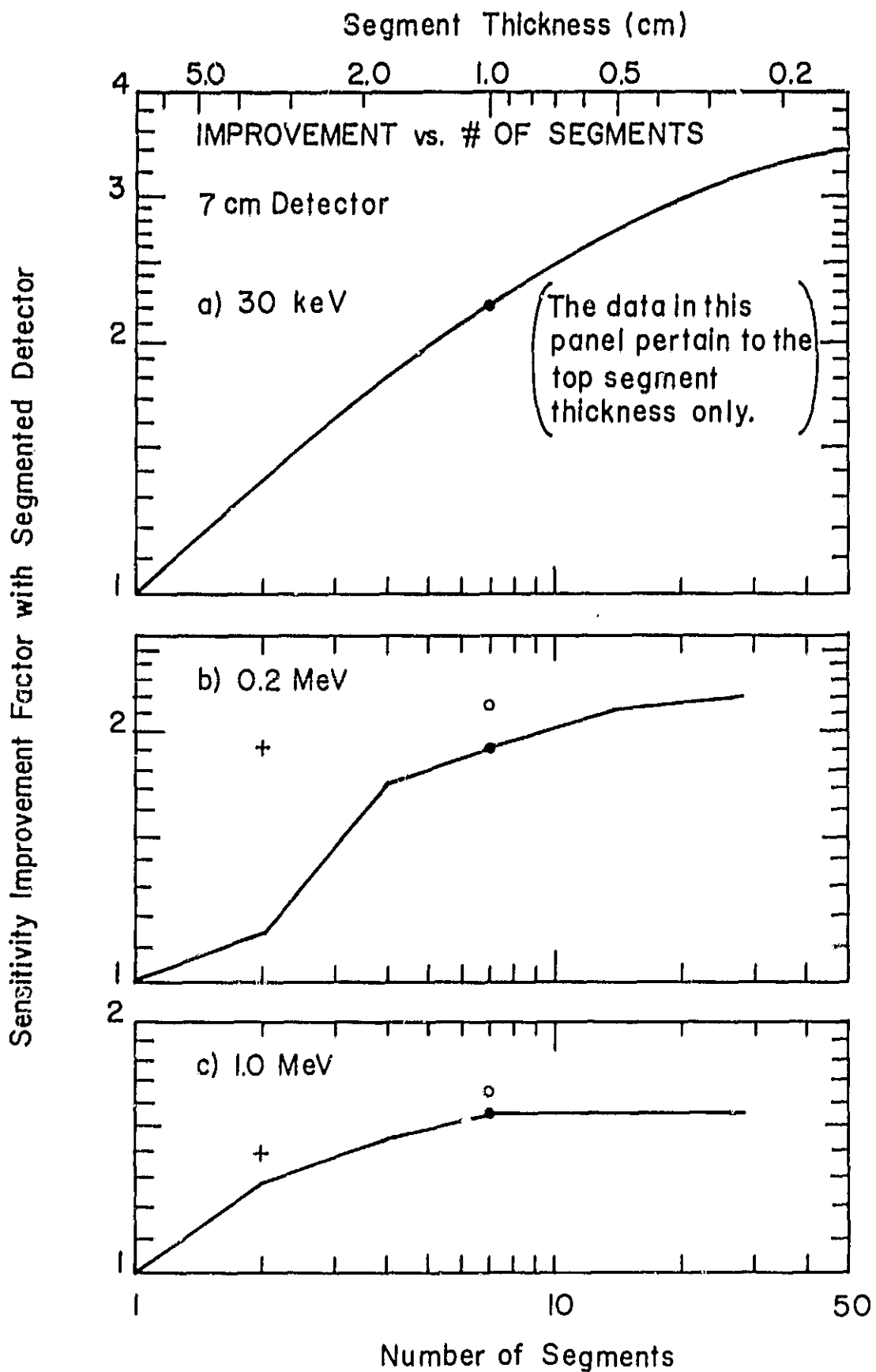


Figure 14

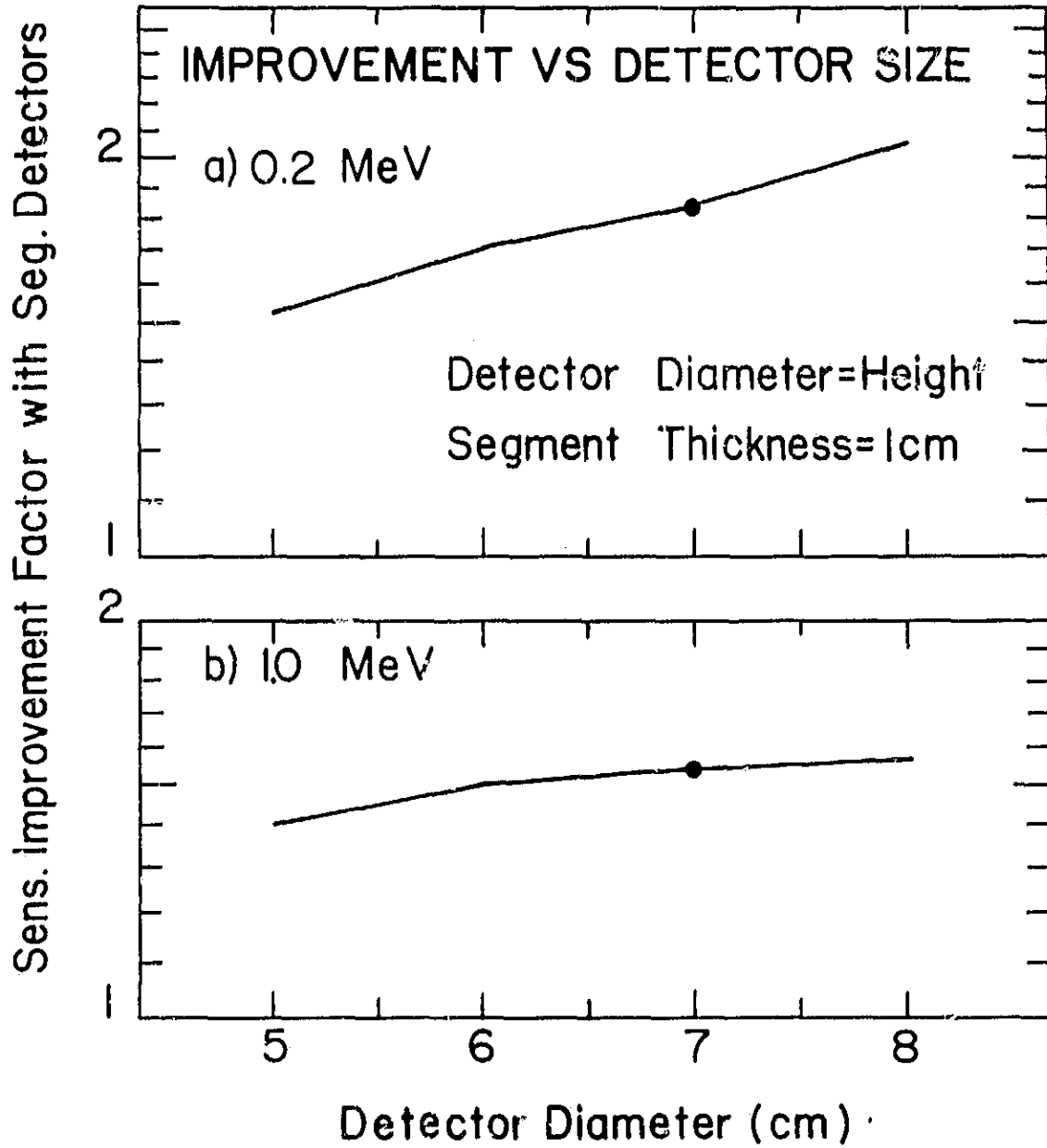


Figure 15

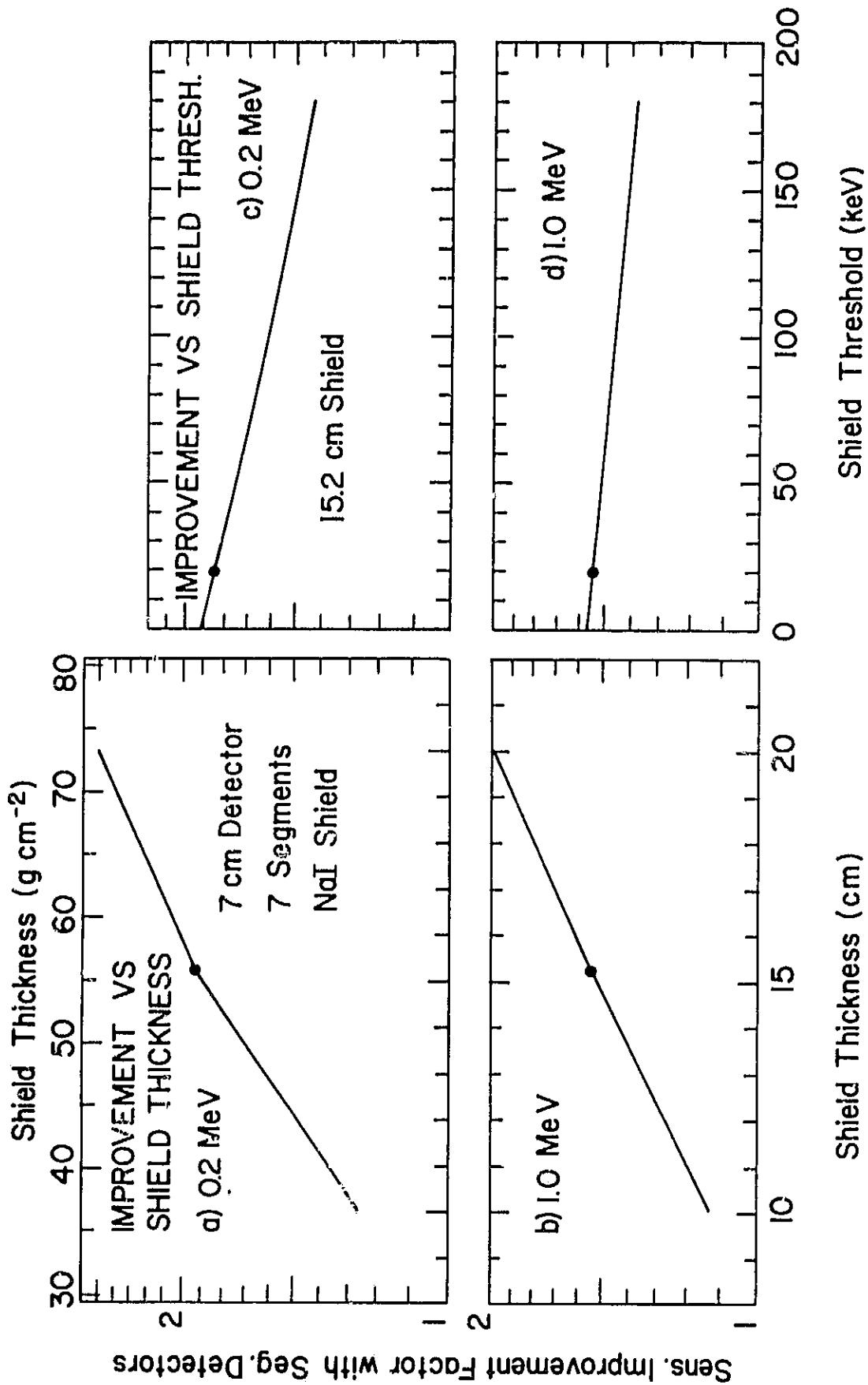


Figure 16

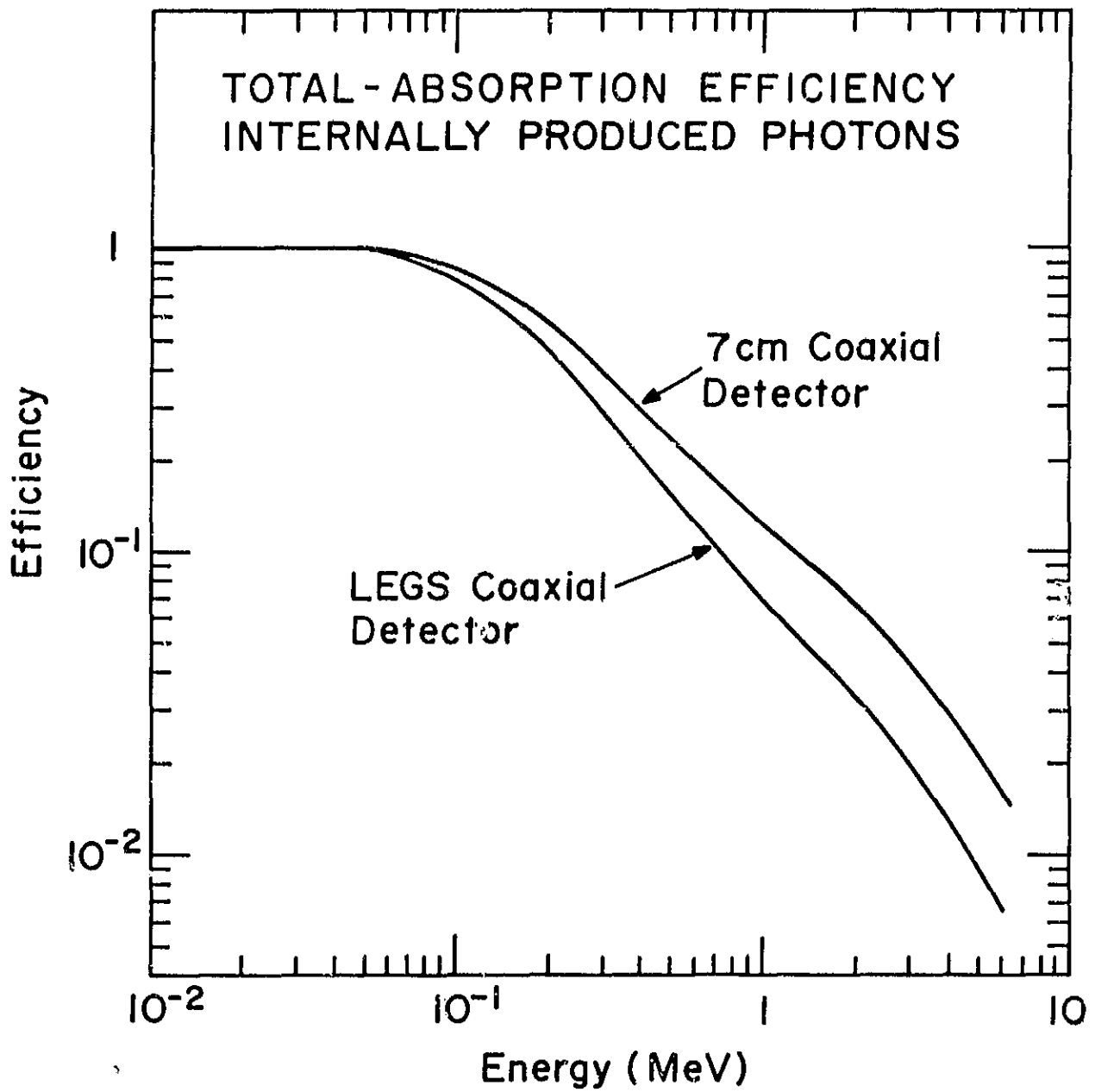


Figure 17

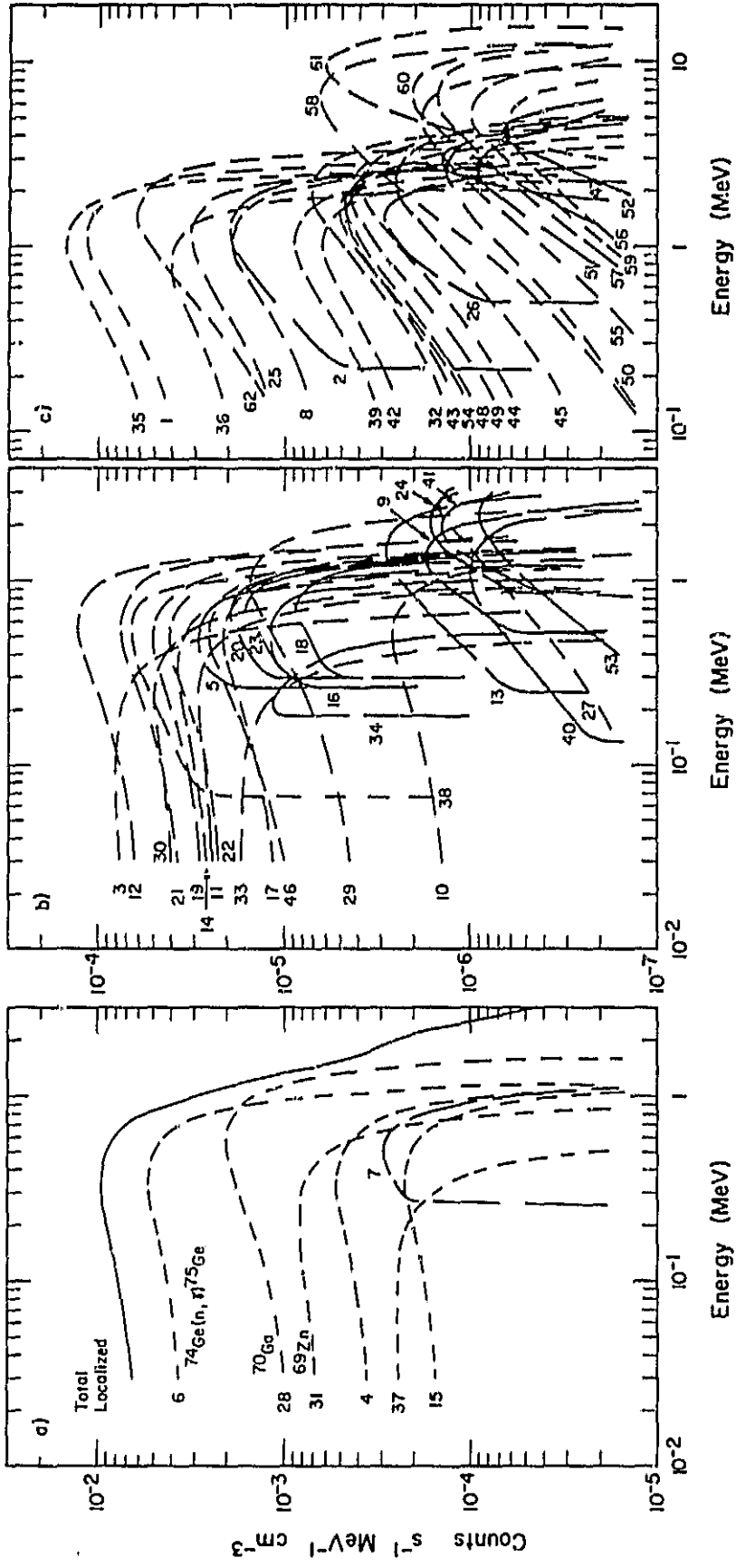


Figure 18